

REMARKS

Claims 1, 3-6 and 8-10 were examined and reported in the Office Action. Claims 1, 3-6 and 8-10 are rejected. Claims 1 and 6 are amended. Claims 1, 3-6, 8-10 remain.

Applicants request reconsideration of the application in view of the following remarks.

I. Drawings

It is asserted in the Office Action that the drawings are objected to because the graph supplied for reference was labeled Fig. 1. The submission of reference drawing Fig. 1 was for the purpose of illustrating the differential thermal analysis resulting in U. S. Patent No. 6,027,833 issued to Ueda et al. and was not intended to replace any application Figures. Accordingly, withdrawal of the objection is respectfully requested.

II. 35 U.S.C. § 112, First Paragraph

A. It is asserted in the Office Action that claims 1, 3-6 and 8-10 are rejected under 35 U.S.C. 112, first paragraph, because the specification, while being enabling for a semi-crystalline structure when boron (B) is present in the carbon shell, does not reasonably provide enablement for such a semi-crystalline structure for the other metal components. Applicant respectfully traverses the aforementioned rejection for the following reasons.

Applicant asserts that the terms "twisting" and "expanding" would be known by an ordinary person skilled in the art. Applicant submits the reference *Adsorption and oxidation of K deposited on graphite*, Surface Science 364(1996) pages 253-265, which asserts such terms known in the art that teaches K belonging to Group 1A intercalates through graphite layers to expand the interlayer distance. Applicant further submits the reference *Synthesis and crystal structure of Al₃BC, the first boridecarbide of aluminum*, Journal of Alloys and Compound 252(1997), pages 98-102, that teaches the twisting structure obtained from carbon and B (refer to Fig. 2 of this reference). Moreover, Applicant submits the reference *Density-functional based tight-binding calculations on zinc-blender type BC₂N-*

crystals, Diamond and Related Materials 7(1998), pages 1633-1638, that teaches several structures of graphite-like BC_2N , that are twisting structures.

And, Applicant asserts that an ordinary person skilled in the art would know that a semi-crystalline structure can be obtained using other metal components based on Applicant's description for a semi-crystalline structure with boron. Applicant describes that elements belonging to Group 3A or 4A of the Periodic Table, such as B, Al, Ga, Si, and Sn, or Group 8 such as Ni, Co, Fe, Mo, and Cr are substituted with one of six-membered carbons in graphite to twist its structure, therefore obtaining a semi-crystalline structure. Additionally, in case of the elements belonging to Group 1A and 2A such as Na, K, Mg, and Ca, the elements may be doped to graphite to expand its structure.

Accordingly, withdrawal of the 35 U.S.C. §112, first paragraph rejection for claims 1, 3-6 and 8-10 are respectfully requested.

B. It is asserted in the Office Action that claims 1, 3-6 and 8-10 are rejected under 35 U.S.C. 112, first paragraph, as failing to comply with the written description requirement due to the limitation "a semi-crystalline structure and at least one shoulder at 700°C or more without a peak at less than 700°C in differential thermal analysis." Applicant respectfully traverses the aforementioned rejection for the following reasons.

Applicant respectfully asserts that the assertion in the Office Action is incorrect because the semi-crystalline structure does not have both crystalline and amorphous forms. Rather the semi-crystalline structure has an intermediate structure that exists between crystalline and amorphous forms. This is supported by Applicant's FIG. 3 illustrating the exothermic peak of the active material according to Example 3. Applicant respectfully points out that in FIG. 3, no peak due to the amorphous carbon occurs at less than 700°C. Therefore, Applicant asserts that independent Claims 1 and 6, which have been amended to recite that the carbon shell has a semi-crystalline structure without a peak at less than 700°C are fully supported by Applicant's original specification. In further support of the above assertions, Applicant submits reference

Anode materials for lithium ion batteries by oxidative treatment of common natural graphite, Solid Stato Ionic 156(2003), pages 283-290 that supports crystalline carbon, graphite, shows only peak, not shoulder at 700°C.

Accordingly, withdrawal of the 35 U.S.C. §112, first paragraph rejection for claims 1, 3-6 and 8-10 are respectfully requested.

C. It is asserted in the Office Action that claims 1, 3-6 and 8-10 are rejected under 35 U.S.C. 112, first paragraph, as failing to comply with the written description requirement due to the limitation "double layer structure." Applicant has amended the claims to remove this limitation to overcome the 35 U.S.C. §112, first paragraph rejection.

Accordingly, withdrawal of the 35 U.S.C. §112, first paragraph rejection for claims 1, 3-6 and 8-10 are respectfully requested.

III. 35 U.S.C. § 112, Second Paragraph

A. It is asserted in the Office Action that claims 1, 3-6 and 8-10 are rejected under 35 U.S.C. 112, second paragraph, as being indefinite for failing to particularly point out and distinctly claim the subject matter which applicant regards as the invention. Applicant has amended claims 1 and 6 to overcome the 35 U.S.C. 112, second paragraph rejection.

Accordingly, withdrawal of the 35 U.S.C. §112, second paragraph rejection for claims 1, 3-6 and 8-10 are respectfully requested.

IV. 35 U.S.C. § 103(a)

It is asserted in the Office Action that claims 1, 3-6 and 8-10 are rejected under 35 U.S.C. § 103(a) as being unpatentable over U.S. Patent No. 6,027,833 issued to Ueda et al. ("Ueda") in view of either U.S. Patent No. 5,595,838 issued to Yamada et al. ("Yamada") or U.S. Patent No. 6,337,159 issued to Peled et al. ("Peled"), and in further view of U.S. Patent No. 5,972,537 issued to Mao et al. ("Mao"). Applicant respectively traverses the aforementioned rejection for the following reasons.

According to MPEP 2142

[t]o establish a prima facie case of obviousness, three basic criteria must be met. First, there must be some suggestion or motivation, either in the references themselves or in the knowledge generally available to one of ordinary skill in the art, to modify the reference or to combine reference teachings. Second, there must be a reasonable expectation of success. Finally, the prior art reference (or references when combined) must teach or suggest all the claim limitations. The teaching or suggestion to make the claimed combination and the reasonable expectation of success must both be found in the prior art, and not based on Applicants' disclosure. (In re Vaeck, 947 F.2d 488, 20 USPQ2d 1438 (Fed. Cir. 1991)).

Applicants' amended claim 1 contains the limitations of

[a] negative active material for a rechargeable lithium battery comprising: a core including crystalline carbon, amorphous carbon or a mixture thereof; and a carbon shell formed around the core, the carbon shell including carbon derived from amorphous carbon and having a semi-crystalline structure and at least one shoulder at 700°C or more without a peak at less than 700°C in differential thermal analysis, and the carbon shell including a metal selected from the group consisting of a transition metal, an alkali metal and an earth metal, and the metal is an elemental metal.

Applicants' amended claim 6 contains the limitations of

[a] negative active material for a rechargeable lithium battery comprising: a core including secondary particles, the secondary particle being prepared by agglomerating at least one primary particle of a crystalline carbon, an amorphous carbon or a mixture thereof; and a carbon shell formed around the core, the carbon shell including carbon derived from amorphous carbon and having a semi-crystalline structure and at least one shoulder at 700°C or more without a peak at less than 700°C in differential thermal analysis, and the carbon shell including a metal selected from the group of consisting of a transition metal, a semi-metal, an alkali metal and an alkali earth metal, and the metal is an elemental metal.

Applicant asserts that claims 1 and 6 limitations of "semi-crystalline" is not amorphous and not crystalline. Applicant submits the references *Evolution of microtexture in furan resin-derived carbon with heat-treatment*, Carbon Vol. 33, No. 10, pages 1377-1381, 1995, and *Electrochemical intercalation of lithium into graphitized carbons*, Solid State Ionics 80(1995), pages 291-298 to support the above-mentioned assertion. It should be noted that the turbostratic structure in the reference paper indicates "semi-crystalline" and is middle stage during the conversion from amorphous carbon to crystalline carbon. Additionally, Applicant notes that the original specification discloses the carbon shell is neither crystalline nor amorphous on page 6, lines 11 to 17.

Ueda discloses a non-aqueous electrolyte secondary cell having a core made of crystalline graphite (carbon) structure. Ueda also discloses that a "low crystallinity or amorphous carbon layer 312 at least partially covering the core 311...." (Ueda, column 8, lines 9-13). The carbon shell disclosed in Ueda is not made of an elemental metal. Unlike the carbon shell of Applicant's claimed invention, the carbon shell disclosed in Ueda has a lower crystallinity, i.e. amorphous carbon.

Ueda does not disclose, teach or suggest a "the carbon shell including carbon derived from amorphous carbon and having a semi-crystalline structure and at least one shoulder at 700°C or more without a peak at less than 700°C in differential thermal analysis, and the carbon shell including a metal selected from the group consisting of a transition metal, an alkali metal and an earth metal, and the metal is an elemental metal."

Yamada discloses a non-aqueous secondary battery arranged having "graphite-like planes [] arranged and stacked in an onion-like shell micro-texture ..." (Yamada, column 3, lines 44-49). Yamada further discloses that the carbon composite electrode includes a crystalline carbon core, a metal film coating the surface of the crystalline carbon core and a carbon layer deposited on the whole surface of the metal film. Yamada does not disclose, teach or suggest

[a] negative active material for a rechargeable lithium battery comprising: a core including crystalline carbon, amorphous carbon or a mixture thereof; and a carbon shell formed around the core, the carbon shell including carbon derived from amorphous carbon and having a semi-crystalline structure and at least one shoulder at 700°C or more without a peak at less than 700°C in differential thermal analysis, and the carbon shell including a metal selected from the group consisting of a transition metal, an alkali metal and an earth metal, and the metal is an elemental metal.

Peled discloses a non-aqueous electrochemical cell arranged having a synthetic passivating layer (SEI) being made of "MACO₃, M₂ CO₃, alkali semi-carbonates, MAO, M₂ O, MAS, M₂S and alkali-and alkaline-earth metal salts of surface carboxylic groups (M=alkali metal, MA=alkaline earth metal). Distinguishable, Applicant's claimed invention has a carbon shell in the form of an elemental metal whereas Peled discloses alkali semi-carbonates, alkali and alkaline earth metal salts, i.e. metal compounds. Applicant's claims 1 and 6 contain the limitation "a metal selected from the group consisting of a transition metal, an alkali metal and an earth metal, and the metal is an elemental metal." Peled, however, discloses the SEI (synthetic passivating layer) of is made of "MACO₃, M₂CO₃, alkali semi-carbonates, MAO, M₂O, MAS, M₂S and alkali-and alkaline-earth metal salts of surface carboxylic groups (M=alkali metal, MA=alkaline earth metal)". In addition, the SEI is formed by preferably bonding the SEI to the surface groups of the carbon particles after the surface groups are formed on the carbon particles.

Further, Peled does not disclose, teach or suggest a

[a] negative active material for a rechargeable lithium battery comprising: a core including crystalline carbon, amorphous carbon or a mixture thereof; and a carbon shell formed around the core, the carbon shell including carbon derived from amorphous carbon and having a semi-crystalline structure and at least one shoulder at 700°C or more without a peak at less than 700°C in differential thermal analysis, and the carbon shell including a metal selected from the group consisting of a transition metal, an

alkali metal and an earth metal, and the metal is an elemental metal.

Mao discloses a method of fabricating a carbon material for use as an electrode in an electrochemical cell. Mao discloses that the "carbon materials are substantially amorphous [and they can also be] partially or completely crystalline or amorphous but possessing crystalline inclusions." (Mao, column 3, lines 6-10). Mao, however, does not teach, disclose or suggest that carbon has a semi-crystalline structure. Further, Mao does not teach, disclose or suggest

[a] negative active material having a double layer structure for a rechargeable lithium battery comprising: a core including crystalline carbon, amorphous carbon or a mixture thereof; and a carbon shell formed around the core, the carbon shell including carbon derived from amorphous carbon and having a semi-crystalline structure and at least one shoulder at 700°C or more without a peak at less than 700°C in differential thermal analysis, and the carbon shell including a metal selected from the group consisting of a transition metal, an alkali metal and an earth metal, and the metal is an elemental metal.

Therefore, even if the teachings of Ueda, Yamada, Peled and Mao were combined, the resulting invention would still not teach, disclose or suggest

[a] negative active material for a rechargeable lithium battery comprising: a core including crystalline carbon, amorphous carbon or a mixture thereof; and a carbon shell formed around the core, the carbon shell including carbon derived from amorphous carbon and having a semi-crystalline structure and at least one shoulder at 700°C or more without a peak at less than 700°C in differential thermal analysis, and the carbon shell including a metal selected from the group consisting of a transition metal, an alkali metal and an earth metal, and the metal is an elemental metal

since neither Ueda, Yamada, Peled, Mao, nor the combination of the four, disclose, teach or suggest all of these limitations. Thus, Applicants' amended claims 1 and 6 are not obvious over Ueda in view of either Yamada or Peled, and further in view of Mao since a *prima facie* case of obviousness has not been met under MPEP 2142.

Additionally, the claims that directly or indirectly depend from Applicant's amended claims 1 and 6, namely claims 2, and 3-5, and 8-10, respectively, are also not obvious over Ueda in view of either Yamada or Peled, and further in view of Mao for the above same reason.

Accordingly, withdrawal of the 35 U.S.C. § 103(a) rejections for claims 1, 3-6 and 8-10 are respectfully requested.

CONCLUSION

In view of the foregoing, it is believed that all claims now pending, namely 1, 3-6, and 8-10, patentably define the subject invention over the prior art of record and are in condition for allowance and such action is earnestly solicited at the earliest possible date.

If necessary, the Commissioner is hereby authorized in this, concurrent and future replies, to charge payment or credit any overpayment to Deposit Account No. 02-2666 for any additional fees required under 37 C.F.R. §§ 1.16 or 1.17, particularly extension of time fees.

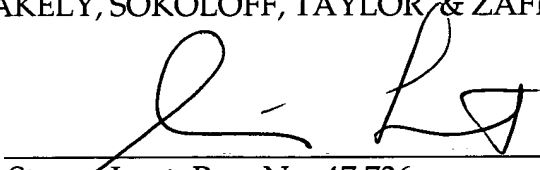
PETITION FOR EXTENSION OF TIME

Per 37 C.F.R. 1.136(a) and in connection with the Office Action mailed on April 20, 2005, Applicant respectfully petitions the Commissioner for a one (1) month extension of time, extending the period for response to August 20, 2005. The Commissioner is hereby authorized to charge payment to Deposit Account No. 02-2666 in the amount of \$120.00 to cover the petition filing fee for a 37 C.F.R. 1.17(a)(1) large entity. A duplicate copy of this sheet is enclosed.

Respectfully submitted,

BLAKELY, SOKOLOFF, TAYLOR & ZAFMAN LLP

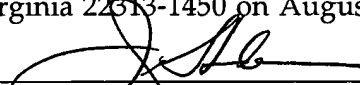
Dated: August 17, 2005

By: 
Steven Laut, Reg. No. 47,736

12400 Wilshire Boulevard
Seventh Floor
Los Angeles, California 90025
(310) 207-3800

CERTIFICATE OF MAILING

I hereby certify that this correspondence is being deposited with the United States Postal Service as First Class Mail with sufficient postage in an envelope addressed to: Mail Stop AF, Commissioner for Patents, P. O. Box 1450, Alexandria, Virginia 22313-1450 on August 17, 2005.


Jean Svoboda



ELSEVIER

Surface Science 364 (1996) 253–265

surface science

Adsorption and oxidation of K deposited on graphite

A. Caballero ^a, J.P. Espinós ^a, A. Fernández ^a, L. Soriano ^b, A.R. González-Elipe ^{a,*}

^a Instituto de Ciencia de Materiales de Sevilla (CSIC-Universidad de Sevilla) and Departamento de Química Inorgánica, PO Box 1115, 41012 Sevilla, Spain

^b Departamento Física Aplicada, Universidad Autónoma, Facultad de Ciencias CXII, Cantoblanco, 28049 Madrid, Spain

Received 11 July 1995; accepted for publication 4 March 1996

Abstract

The bonding state of K intercalated in highly oriented pyrolytic graphite (HOPG) has been studied by X-ray photoelectron spectroscopy (XPS) and X-ray absorption fine structure/near-edge X-ray absorption fine structure (SEXAFS/NEXAFS) spectroscopies. Intercalation of potassium into HOPG occurs at room temperature after deposition on its surface by evaporation from a getter source. In this state XPS and angle-resolved NEXAFS at the K 1s edge show the existence of a transfer of charge from the potassium to the graphite layers and provide some clues about the hybridization of the p states of K with the σ^* and π^* empty states of the graphite layers. Meanwhile, SEXAFS shows that the K atoms are placed at the centre of the hexagon units of an expanded and reordered graphite structure.

Adsorption of 80 L of oxygen at 298 K on K-HOPG produces changes in the shape and intensity of the K 2p photoelectron peak, while the width and asymmetry of the C 1s peak decrease. The progressive incorporation of oxygen into the system is monitored by the development of an O 1s peak with a binding energy between 531.3 and 531.8 eV. In all cases, a rough estimation of the O/K ratio calculated from the areas of the O 1s and K 2p peaks gives values around one. Further changes in the same direction at the K 2p and C 1s photoelectron peaks and an additional increase in the amount of incorporated oxygen occur after adsorption of oxygen at 373 K. Similarly, under these conditions the calculated O/K ratio remains close to one.

The SEXAFS spectra after adsorption of oxygen are similar to those obtained before adsorption, except for a general and small decrease of the intensity of the EXAFS oscillations. Fitting analysis of the spectra provides the same C–K distance and N_{30}/N_{70} ratio ($N_{30,70}$: apparent coordination numbers measured at incident angles of the radiation of 30° and 70° in respect to the surface normal) as before adsorption of oxygen. However, there is a decrease of ~45% in the absolute values of N in respect to the original sample. NEXAFS spectra at grazing incidence are also similar but depict a new feature when recorded at normal incidence. The intensity of this feature increases with the amount of incorporated oxygen.

The model proposed to explain these results assumes that adsorption of oxygen produces a depletion of the negative charge in the graphite layer and the formation of O_2^- species at the surface (δ likely to be two). Simultaneously, the adsorption of oxygen at 298 and 373 K induces the partial segregation of the intercalated potassium to the external surface of the HOPG crystal where it becomes associated to the adsorbed oxygen. In this state SEXAFS spectra are dominated by the potassium still intercalated within the layers, while XPS is more sensitive to the atoms segregated to the surface.

Keywords: Alkali metals; Graphite; Near edge extended X-ray absorption fine structure (NEXAFS); Oxidation; Surface extended X-ray absorption fine structure (SEXAFS); X-ray photoelectron spectroscopy

* Corresponding author. Fax: +34 5 4611962; e-mail: agustin@cica.es

1. Introduction

The characterization of the adsorption state of alkaline metal (AM) on different substrates is a subject of great interest because of its implications in a large variety of fields including catalysis, electronics, AM-doped fullerenes [1,2], etc. In past years the study of the adsorption of AMs on graphite has been of particular relevance [3–15]. Intercalation compounds have been extensively studied by different techniques including EXAFS [16,17]. The use of surface science techniques, specially when using highly oriented pyrolytic graphite (HOPG), has been a very fruitful approach in characterizing the adsorption state of AMs. Thus, the geometry of the adsorption site and their long-term arrangement have been studied by low energy electron diffraction (LEED) [3–5], HREELS or He diffraction [10–13], while the electronic characteristics of the bond have been explored by means of valence band and core level photoemission [6–8]. Also, similar studies have been carried out in the emerging area of fullerenes doped with AMs, where valence band and core level photoemission [2,18,19] have contributed to the understanding of their electronic properties and reactivity. Owing to the obvious similarities of fullerene-AM and HOPG-AM systems, the study of the latter, especially in an intercalation arrangement, is of interest in understanding the bonding characteristics of AM in fullerenes.

However, the interaction of AMs with HOPG and their reactivity with simple molecules such as O_2 , H_2 , etc., are not yet clear. In this respect, the behaviour of AM-HOPG systems as a function of temperature is not well known. Thus, referring to K-HOPG, it has been shown that potassium evaporated at low temperature remains adsorbed on the surface of HOPG, while at 298 K it intercalates through its external layers [4,10–15]. The intercalation geometry of K into HOPG has been thoroughly studied by means of LEED by Ignatiev et al. [4]. The most important results of this study, in connection with the experiments carried out here, are that the layer distance of HOPG expands to a value of $d = 5.35 \text{ \AA}$ and the AB configuration of the layers (i.e. the C atoms of a layer are placed at the centre of the hexagon units of the subsequent

layer) changes to AA (i.e. the C atoms of a layer are placed on the top position of the atoms of subsequent layers). Also of special relevance for the present paper are previous studies by Hughes et al. [6–8] by angle-resolved photoemission (ARP) and XPS, in which these authors showed that approximately one electron charge per intercalated potassium is transferred to graphite. These ARP results are in good agreement with theoretical investigations on this system [20–22]. However, the transfer of charge seems smaller when, at low temperature, potassium remains adsorbed on the surface of HOPG.

The study of the reactivity of C-AM systems with simple molecules or atoms is an interesting approach to understanding its bonding state. This has been recently shown by Ohno et al. [23] in a photoemission study of K-doped fullerene subjected to the action of a beam of H atoms and by Molodtsov et al. [18] by looking into the effect of oxygen on K-doped fullerene. More related to our present study, it has been shown that in Cs deposited on graphite, the adsorption of oxygen changes the work function of the system [9,24]. Very recently, it has also been shown that in an intercalation compound, Cs-graphite, the adsorption of oxygen produces a partial segregation of Cs to the surface where it becomes oxidized [25].

With the present paper we want to contribute to the characterization of the intercalation state of K in HOPG as well as to the study of the reactivity of such intercalated systems with O_2 . We have used XPS and X-ray absorption (EXAFS/NEXAFS) spectroscopies. The obtained results have confirmed the intercalation geometry of K proposed previously by Ignatiev et al. [4]. In addition, we have shown that by reaction of K-HOPG with oxygen at 298 and 373 K there is a partial segregation of potassium to the surface of HOPG where it becomes associated with adsorbed species of oxygen.

2. Experimental

Potassium was deposited on HOPG by evaporation from a getter source (SAES). Before each

evaporation the graphite crystal was cleaved in air with a scotch tape and then heated in ultrahigh vacuum (UHV) at 673 K for 2 h. This treatment removes any trace of oxygen or other contamination from the surface of the graphite. Previous to the potassium evaporation, the getter source was carefully outgassed under UHV. A maximum pressure of 1×10^{-9} Torr was reached during evaporation. Light hydrocarbons (CH_4 , C_2H_6) and CO were the gas species detected by mass spectrometry.

The measurements reported in this paper were carried out with the sample at room temperature in two different UHV chambers. The first one, in our laboratory in Seville, was an Escalab 210 system from VG, supplied with a X-ray gun and a hemispherical analyzer. In this chamber a base pressure of 1×10^{-10} Torr was reached routinely. The XPS spectra were recorded by excitation with non monochromatic $\text{MgK}\alpha$ radiation, while the electron energy analyzer was working in the constant pass energy mode at 50 eV. The sample was grounded during analysis and the binding energy scale of the spectra was not charge corrected. Atomic ratios were calculated from the area of the photoelectron peaks corrected with their empirical sensitivity factors.

In the second chamber we measured the SEXAFS/NEXAFS spectra of potassium deposited on graphite. It was installed at the station 6.3 of Daresbury Laboratory. Potassium K-edge (~ 3609 eV) spectra were excited by the light from a Ge(111) double-crystal monochromator. Although the K_{LMM} Auger yield was measured in some cases with a double-pass cylindrical mirror analyzer (CMA)(Physical Electronics) operated in the non-retardation mode, all the reported spectra were collected by measuring the drain current through the sample (total yield, TY). No differences in the shape of the spectra were found between these two detection modes. Normalization of the SEXAFS/NEXAFS data to incident photon flux was done by means of the electron yield measured at a metal reference placed between the monochromator and the sample chamber. During measurements the base pressure in this chamber was $\sim 2 \times 10^{-10}$, although it increased to $\sim 10^{-9}$ during K evaporation.

The same kind of experiment was carried out in the two chambers. It consisted of the evaporation of K on a cleaned HOPG sample, then the exposure at 298 K to O_2 up to a maximum dose of 80 L and finally heating at 373 K while exposing again to 80 L of O_2 . In the samples exposed to potassium, any possible contamination with oxygen was checked by recording photoemission spectra through the O 1s and O_{AES} regions.

The amount of potassium deposited on graphite was estimated from the intensity of the K 2p and C 1s photoemission peaks. The experiments were generally carried out for low nominal coverages of K, typically around 0.5–1 equivalent monolayers. Since potassium diffuses within the graphite layers up to an unknown depth and then, on oxidation, segregates partially to the surface (see Section 3 and Section 4), neither the use of “monolayers” or “atomic ratios” is appropriate to quantify the XPS spectra. Nevertheless, we used the second type of magnitude because it is easy to calculate and, after exposure of the system to oxygen, it reflects very clearly the enrichment in potassium of the outermost layers of the graphite.

The spectra were analysed with the software package developed by Bonnin et al. [26]. The coordination numbers (N), distances (R), and Debye–Waller factors (σ) were extracted by a least-square fitting procedure that uses the theoretical phases and amplitudes proposed by Rehr et al. [27].

3. Results

Fig. 1 shows K 2p and C 1s XPS spectra, before and after deposition of potassium and after exposure of the system to 80 L of O_2 at room temperature and then 373 K. After the deposition of K, the C 1s peak broadens and becomes more asymmetric, while the binding energy (BE) position of its maximum shifts from 283.8 to 284.2 eV. Broadening and peak asymmetry revert only partially after exposure to O_2 . In Table 1 we summarize the values of the full width at the half maximum (FWHM) of the C 1s peak and the BE measured at its maximum corresponding to the four situa-

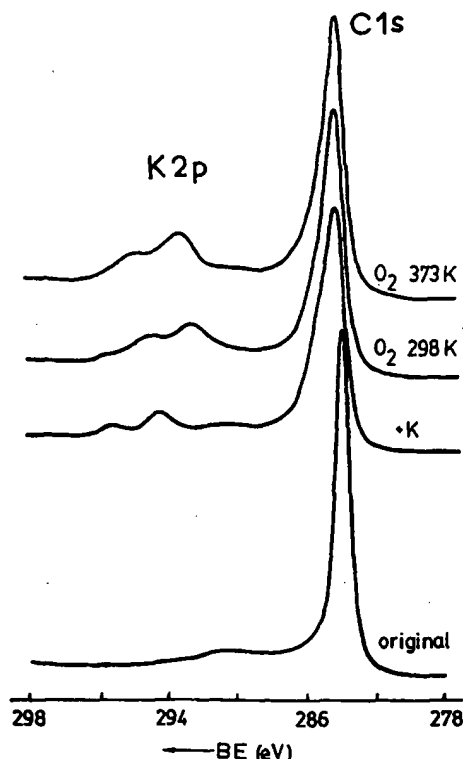


Fig. 1. K 2p and C 1s XPS spectra of HOPG. (a) Original sample; (b) after deposition of metallic potassium; (c) system exposed to 80 L of oxygen at 300 K (d) system exposed to 80 L of oxygen at 373 K.

Table 1
Peak parameters deduced from photoelectron spectra

Sample	C 1s		K 2p _{3/2} ^b BE (eV)	O/K	C/K
	BE (eV)	FWHM ^a (eV)			
HOPG	283.8	1.6	—	—	—
HOPG+K	284.2	3.2	294.6	—	23
HOPG+K+O ₂ (298 K)	284.2	2.6	292.7	0.8	15
HOPG+K+O ₂ (373 K)	284.2	2.4	293.4	1.1	12

^a Full width at half maximum.

^b Position of the experimental maxima

tions of the sample whose spectra are in Fig. 1. In Table 1 we have also summarized the BE positions of the experimental maxima of the K 2p_{3/2} peaks,

as well as the O/K ratios measured after the different exposures to O₂.

The values of the atomic ratios in this table show a progressive and parallel enrichment of the surface in potassium and oxygen, the O/K ratios remaining in all cases close to one. In these experiments the O 1s band develops a broad shape with a maximum that shifts progressively from 531.3 to 531.8 eV. It is also interesting that at 298 K exposure to 80 L of O₂ is enough to saturate the system in oxygen. This was proved because at this temperature no significant changes in the K 2p and O 1s signals were observed after a prolonged exposure to 6x10³ L of O₂.

A more detailed analysis of the K 2p spectra after exposure to different doses of O₂ is shown in Fig. 2. The fitting analysis of these spectra reveals that they are formed by three different forms of potassium. The first one, at 294.6 eV, corresponds to "elemental" potassium. This form is always present in the experimental signal (spectra a–f in Fig. 2). The second form, characterized by a band

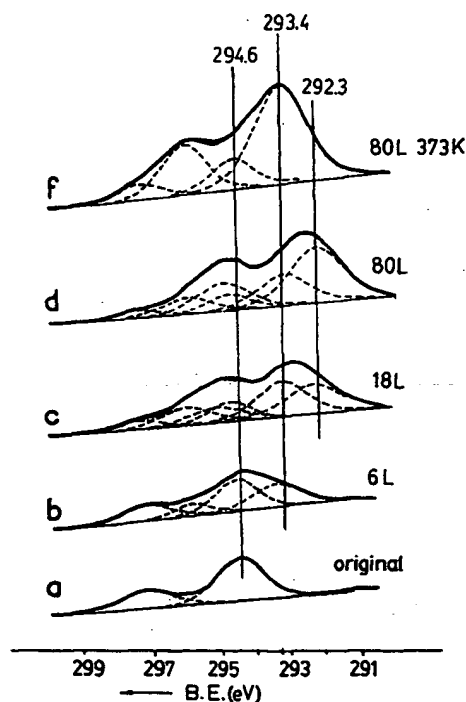


Fig. 2. K 2p fitted photoelectron spectra corresponding to those in Fig. 1 for K deposited on HOPG and then exposed to the indicated dose of O₂.

at 293.4 eV, appears after exposure to 6 L of O₂ (spectrum b). It increases in intensity for larger doses of O₂ at 298 K and 373 K (spectra c–f). The third form of potassium is characterized by a BE of 292.3 eV. It develops after exposure to O₂ at 298 K (spectra c and d), but disappears in spectrum f recorded after dosing O₂ at 373 K. It is also apparent from the spectra in Fig. 2 that the overall increase in the intensity of the K 2p signal is due to the forms with K 2p_{3/2} BE of 292.3 and 293.4 eV, which must correspond to oxidized potassium associated with some oxygen species [28–31].

A similar experiment was carried out by recording the X-ray absorption spectra of the K 1s edge for grazing and normal incidences. Fig. 3 shows these spectra for the K-HOPG sample before adsorption of oxygen. The high signal-to-noise ratio of these spectra permits their analysis either at the NEXAFS and EXAFS regions.

Fig. 4 shows the potassium K-edge NEXAFS spectra at different incident angles between 90 and 20°. The spectrum at normal position (i.e. $\theta = 90^\circ$) is characterized by a sharp edge with a leading peak at approximately 5 eV above the threshold and a shoulder at about 18 eV from it (we take the jump edge at ~ 3604 eV by linear extrapolation of the absorption jump up to zero absorption).

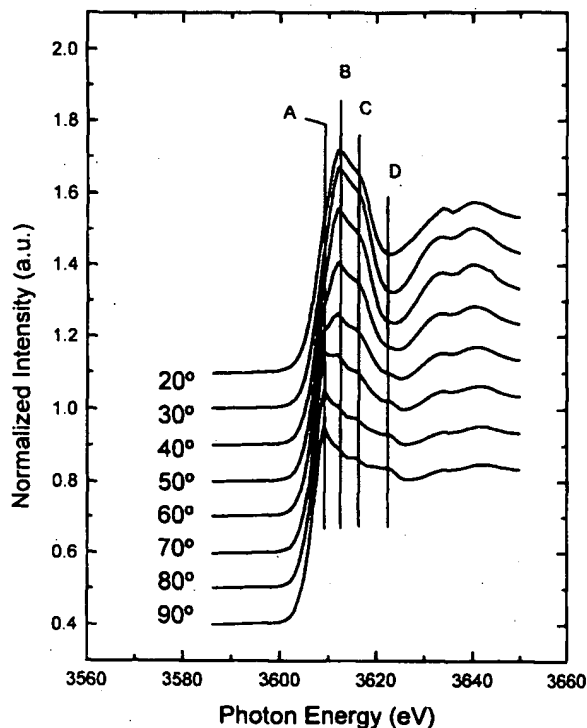


Fig. 4. Potassium K-edge NEXAFS spectra at different incident angles for an HOPG crystal with potassium deposited at 298 K.

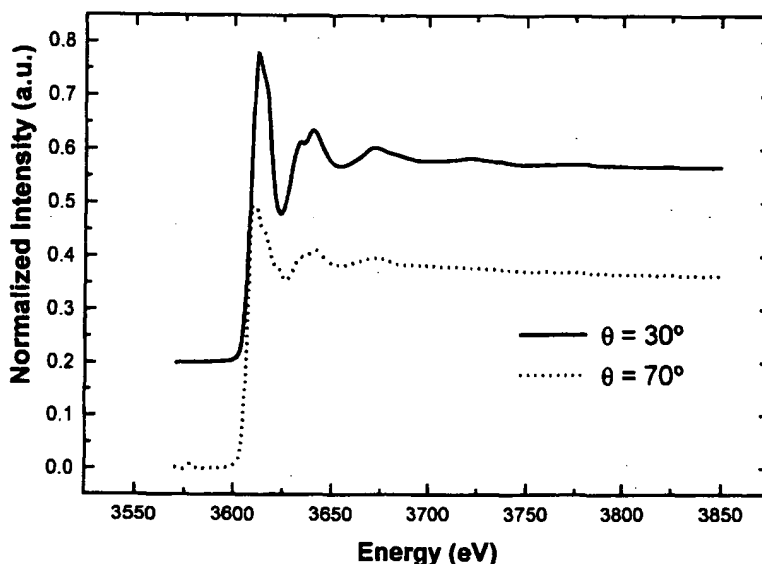


Fig. 3. Potassium K-edge X-ray absorption spectra at grazing (30°) and normal (70°) incidence positions for an HOPG crystal doped with K.

However, when the incident angle of the radiation is more grazing, two new features dominate the spectra as clearly seen at incident angles of 30 or 20°. In the following these features are referred to as A (3609 eV), B (3612 eV), C (3617 eV) and D (3622 eV).

After exposure to O₂, there are only some minor changes in the XANES spectra. Fig. 5 shows the spectra taken at different incident angles of radiation after the exposure of the graphite sample with potassium to 80 L of oxygen at 373 K. It is interesting that at grazing incidence the spectra before (Fig. 4) and after (Fig. 5) exposure to O₂ are similar, except that the height of features B and C in respect to the base line defined by the EXAFS oscillations is slightly smaller after adsorption of O₂. Also important in this series of spectra is the appearance of a new feature at 3617 (E) that presents its maximum intensity at normal incidence. It must be noted that although features C

and E have a similar energy they show different behaviours with respect to the incident angle of radiation. Feature E, has a maximum intensity at normal incidence and therefore it must correspond to an electronic state with a symmetry parallel to the layer planes of the graphite structure. On the contrary, features B and C must correspond to states with a perpendicular symmetry in respect to these planes. Spectra similar to those shown in Fig. 4 were obtained after dosing O₂ at 298 K. However, the intensity of feature E was smaller. In general, at 298 K the intensity of feature E at normal incidence grew continuously with the doses of oxygen up to saturation (i.e. 80 L). A further increase to reach its maximum intensity was obtained in the experiment at 373 K.

The SEXAFS region was recorded simultaneously to the NEXAFS. The EXAFS functions, corresponding to the K-HOPG sample, were extracted from the spectra in Fig. 3 after background removal. An example of the quality of the data and the relative intensity of the EXAFS oscillations is shown in Fig. 6. The FT curves are characterized by a main peak at $R \approx 2.8$ and a shoulder at about 4.0. No well-defined peak can be observed beyond this value. Fitting analysis of the spectra was carried out after back-Fourier transformation of the range 0–4.5 (i.e. including the main peak and the shoulder). Fig. 7 shows the FT curves obtained at grazing ($\theta = 30^\circ$) and normal ($\theta = 70^\circ$) incidences for the K-HOPG sample before and after exposure to O₂ at 298 and 373 K. The figure also includes the curves obtained by fitting analysis (dotted lines). A good fitting of the first maximum of the FT curve is only possible under the assumption that only carbon atoms form the first coordination sphere of K. The best reproduction of the shoulder of the FTs is obtained by assuming that the second coordination sphere around K is also formed by C atoms. However, here, owing to the low intensity of this feature, the fitting parameters are subjected to large errors. Therefore, we will concentrate the discussion on the best-fitting parameters of the main peak of the FT curves. Table 2 summarizes the values of these fitting parameters. From this table it appears that the calculated N_{30}/N_{70} ratio is 2.60, a value close to the theoretical value of 3.25 obtained for a

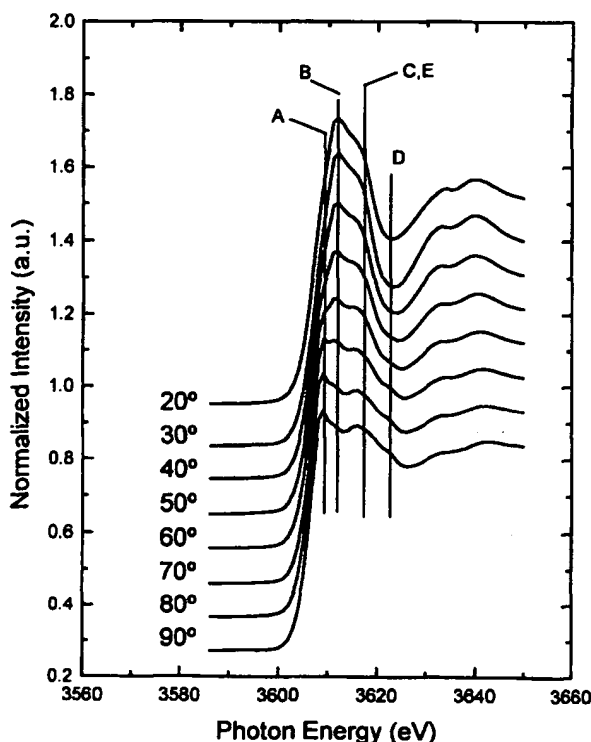


Fig. 5. Potassium K-edge NEXAFS spectra at different incident angles for an HOPG crystal doped with K and then exposed to 80 L O₂ at 373 K.

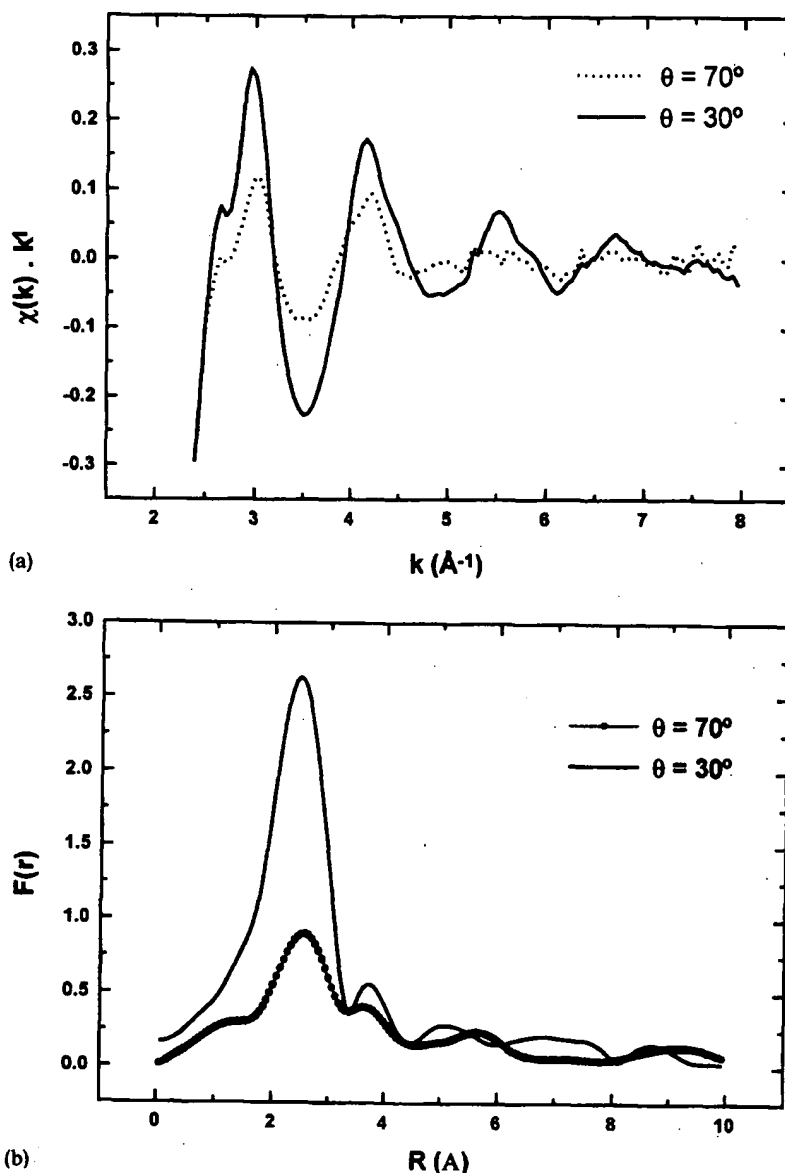


Fig. 6. Potassium K-edge EXAFS (top) and FT curves (bottom) at normal (70°) and grazing (30°) angles of incidence for an HOPG crystal doped with K.

potassium atom placed at the centre of the hexagonal units that form the layers of graphite (see Appendix A; the difference between experimental and theoretical values is not significant if one takes into account that fitting is always subjected to uncertainties and that an experimental error of just two degrees in θ would be enough to produce

very significant deviations in the experimental N_{30}/N_{70} ratio).

On the other hand, except for the absolute values of N that decrease up to 45% at 373 K, the other fitting parameters do not change significantly after exposure of the system to O_2 (see the K–C distances and Debye–Waller factors in Table 2). Also, the

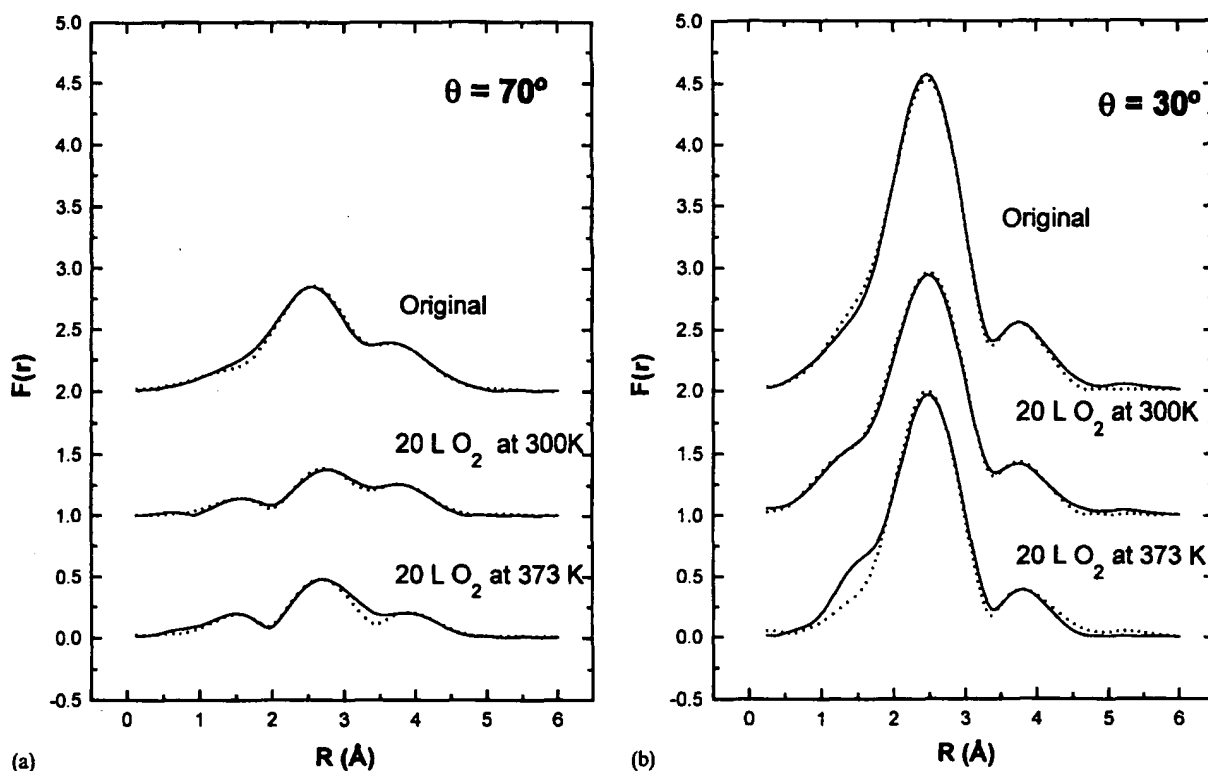


Fig. 7. FTs (full line) and curves obtained by fitting (dotted lines) for HOPG doped with potassium and then exposed to O_2 at 298 K and 373 K.

measured N_{30}/N_{70} ratios after O_2 adsorption can be taken as similar to the ratio before adsorption.

4. Discussion

4.1. Intercalation of potassium

The adsorption of K on the surface of single crystal or HOPG samples has been the subject of many studies during the last ten years. At low temperatures it appears that potassium remains adsorbed on the surface of graphite. This adsorption has been studied as a function of coverage by LEED [12,13], He diffraction [12,13] and HREELS [10,11,14,15].

Ignatiev et al. [4], in an early study by energy-dependent LEED, recognized that the deposition of potassium at room temperature leads to the intercalation of the metal within the most external

layers of graphite. The expansion of the interlayer distance to 5.35 \AA and the transfer to the layer of almost one electron charge per intercalated atom of potassium are characteristic features of this intercalated state as determined by LEED [4] and photoemission experiments [6]. In our case, potassium was deposited at room temperature and therefore intercalation of the potassium atoms within the external layers of graphite should be expected. Our XPS and EXAFS/NEXAFS results confirm the intercalated state of potassium and the existence of a transfer of charge from the potassium to the graphite. In fact, the N_{30}/N_{70} ratio of 2.6 calculated from the fitting parameters of the EXAFS spectra at grazing and normal incidences is reasonably close to the theoretical value of 3.25 calculated for an intercalated geometry where the potassium is placed between two hexagons of C atoms (see Appendix A). Moreover, the value of the K–C distance (i.e. $\sim 3.0 \text{\AA}$) determined by

Table 2
Best-fitting parameters of the potassium K-edge EXAFS spectra

Sample	normal incidence ($\theta = 70^\circ$)				grazing incidence ($\theta = 30^\circ$)			
	R (Å) ^a	N ^b	σ^c (Å)	E (eV)	R (Å)	N	σ (Å)	E (eV)
HOPG + K	3.058	3.7	0.125	6.22	2.994	9.6	0.124	6.63
O ₂ (298 K)	3.166	2.0	0.122	6.30	2.998	8.3	0.138	6.37
O ₂ (373 K)	3.057	2.3	0.120	6.19	2.994	5.5	0.104	6.26

^a Apparent interatomic K–C distance.

^b Coordination number.

^c Debye–Waller factor.

EXAFS analysis and the fact that only one K–C distance is obtained for the first coordination sphere are two facts that support the displacement of one layer of graphite in respect to the other to form an A–A stacking arrangement. The value of this expanded interplanar geometry is 5.34 Å, which is compatible with the obtained K–C distance and similar to the value obtained by LEED by Ignatiev et al. (e.g. 5.35 Å) [4] for K intercalated in graphite.

On the other hand, XPS has shown that after deposition of potassium the C 1s peak broadens and becomes more asymmetric. According to the model of Donian–Sunyik [32] for the line shape of photoelectron peaks of conducting materials, the broadening and asymmetry of core level peaks depend on the density of free electrons close to the Fermi level. Therefore we can conclude that after deposition of potassium the concentration of free electrons in the graphite layers increases because of a charge transfer from the potassium to the graphite.

NEXAFS spectroscopy probes the unoccupied electronic states of the absorbing atom above the Fermi level of the material. According to the dipole transition rules, the spectra in Fig. 2 correspond to a K 1s→K 4p electron transition. Therefore the different peaks observed in the spectrum must involve K 4p unoccupied states of potassium. The most intense and differentiated features in the spectra depict a different behaviour as a function of the incident angle of the radiation. Features A and D present their maximum intensity at normal incidence while features B and C present their maximum intensity at grazing incidence. This

behaviour suggests that feature A, the most intense at normal incidence, is associated with p states with a symmetry parallel to the plane of the layers. On the other hand, according to the results of the EXAFS analysis, potassium is only bonded with C and there are no other potassium atoms in the interlayer space located at bonding distances. It is likely therefore that feature A corresponds to bonding p orbitals of potassium directed parallel to the layers. On the contrary, features B and C have their maximum intensity at grazing incidence. Therefore, they correspond to p orbitals of K with a perpendicular symmetry with respect to the layers of graphite. In this case, it should be expected the hybridization of these orbitals with available states of the graphite layers. In this respect it is interesting that the energy separation between the σ^* and π^* empty orbitals of graphite, both of p character, is approximately 5 eV, as determined by EELS [33]. This energy separation is similar to that existing between features B and C of the NEXAFS spectrum. We think that these two features correspond to empty states resulting from the hybridization of the 4p_z orbital of potassium with the σ^* and π^* empty states of graphite. Previous NEXAFS studies on Cs intercalated on graphite have also shown the appearance of structures correlated with p_x, p_y and p_z final states located on Cs sites [17].

4.2. Reaction with oxygen

The reaction with oxygen of alkaline metals adsorbed or intercalated in graphite has been studied previously by photoemission for

K-graphite and other systems [9,14,15,28–31,34]. Our results by XPS show that exposure of K-HOPG to O_2 at room temperature (spectrum b in Fig. 1) produces a shift in the K 2p peak position to a lower BE than in the original samples. Simultaneously, the width of the C 1s peak slightly decreases and becomes less asymmetric (cf. Table 1). Sharpening of the C 1s peak must be associated with a partial removal of the density of charge initially transferred to the graphite layers from the intercalated atoms of potassium. Since on adsorption of oxygen the C 1s peak did not recover completely its initial shape and position before deposition of potassium, we can conclude that only a part of this electronic charge is transferred to the oxygen. It is likely that the transfer of charge and segregation of potassium occur mainly from the uppermost layers of the graphite. Therefore the experimental C 1s signal should be a convolution of the contribution of these layers with very little or no intercalated potassium and that of the deeper zones of the sample where K still remains intercalated.

On the other hand, the fitting analysis of the K 2p spectra has shown the formation of two different forms of oxidized potassium characterized by BEs at 292.3 and 293.4 eV [28–31] and the simultaneous development of a broad O 1s peak with a BE shifting from 531.3 to 531.8 eV as the amount of adsorbed oxygen increases. This range of BE values is consistent with the formation of O_2^{2-} species associated with oxidized atoms of K [35,36]. Moreover, the measured O/K ratios close to one, supports the formation of a kind of O_2^{2-} species under our experimental conditions (i.e. stoichiometry of the oxide close to K_2O_2 , although the XPS spectrum shows the presence of some unreacted potassium). The assignment of the bands at 294.6 and 293.4 eV to elemental potassium intercalated within the graphite layers and to oxidized potassium at the surface of graphite is consistent with previous results in the literature for potassium adsorbed and oxidized on the surface of different substrates [28–31]. In most of these studies a shift between 1 and 1.5 eV to lower BE in the position of the K $2p_{3/2}$ peak is reported upon oxidation. Here, a form of potassium characterized by a K $2p_{3/2}$ BE of 292.3 eV (i.e. shifted by 2.3 eV in

respect to elemental potassium) appears at the initial stages of the oxidation. A general observation for an alkaline metal intercalated in graphite is that, for the first steps of exposure to oxygen, the binding energy of the oxidized forms decreases with increasing oxidation [29]. On oxidation shifts in the BE positions for Cs on carbon have been attributed to work-function changes [9]. Tentatively, we propose that the form at 292.3 eV corresponds to isolated potassium–oxygen species. The progressive oxidation by heating at 373 K, besides inducing a further segregation of potassium to the surface (see below), could favour the aggregation of the $K^+O_2^{2-}$ species into potassium peroxide clusters covering part of the graphite surface and then inducing the shift to 293.4 eV. Nevertheless, a most interesting point to note from the XPS study is that at 298 K there is a progressive increase in the overall intensity of the K and O signals with doses of O_2 up to saturation with 80 L. The further increase obtained by dosing oxygen at 373 K shows that the incorporation of oxygen and the simultaneous segregation of K to the surface are enhanced by thermal activation. It is also interesting that at 373 K the K $2p_{3/2}$ spectrum still contains a contribution peak at around 294.6 eV due to elemental potassium.

Despite this extensive oxidation of potassium deduced from the analysis of the K 2p and O 1s spectra, the NEXAFS/SEXAFS spectra do not show such large changes as those observed by XPS. In fact, the C–K distances and, within the accuracy of the method, the N_{30}/N_{70} ratios are similar to those obtained for the sample before O_2 adsorption. This shows that even at 373 K there is still a large set of K atoms intercalated between the graphite layers where they present the same geometry as before adsorption of oxygen. This potassium must be responsible for the doublet at 294.8 eV detected in the XPS spectra even after the experiment at 373 K. However, the systematic decrease in the absolute values of N as the oxidation progresses indicates that a certain number of the initially intercalated atoms has lost this geometrical arrangement. The lack of any new clear feature in the FTs associated to a K–O bond might indicate a large dispersion of bond distances and/or angles leading to the self-cancellation of the corre-

sponding EXAFS oscillations. Owing to the fact that amplitude and phase shift functions are similar for K–O and K–C bonds, the observed decrease might be also consistent with the change of coordination from twelve C atoms to a much smaller number of O atoms when the potassium segregates to the surface, provided that bond distances are similar. At 373 K the amount of segregated potassium, estimated from the decrease in N , is approximately 45% of the number of potassium atoms. All these results by XPS and SEXAFS can be accounted for by assuming that on adsorption of O_2 a part of the potassium segregates to the surface of the HOPG sample where it becomes oxidized. The different sampling depth of these two techniques explains why the former shows the almost full oxidation of the potassium (spectrum f in Fig. 2), while the latter shows that only 45% of the potassium atoms have lost the intercalated arrangement. A similar process has recently been described by Vayer-Besançon et al. [25] for an intercalation compound of Cs into graphite and by Rousseau et al. [29] for K-, Rb- and Cs-intercalated compounds. Sjövall et al. [14,15] have also suggested a similar process based on HRELS and TDS experiments with K-graphite.

In agreement with the previous view the NEXAFS spectra after adsorption of oxygen show very little change in respect to the spectra before adsorption. Therefore the experimental NEXAFS spectra result from the superposition of the spectra of the intercalated and oxidized potassium atoms. Feature E at normal incidence is the only indication of a partial oxidation of potassium. According to the dipole transition rules this feature must involve 4 p empty states of potassium hybridized with available states of oxygen with a symmetry parallel to the planes of graphite. This suggests that the potassium oxide segregated to the surface forms an overlayer with potassium–oxygen bonds parallel to the graphite layers.

At grazing incidence it appears that the K–O bonds do not contribute to the NEXAFS spectra that are still characterized by the presence of the same features B and C that appeared in the spectra before adsorption of O_2 . However, in this case, their intensity, referred to the height of the base

line of the EXAFS region, decreases in agreement with the loss of intercalated potassium.

5. Conclusions

From our experiments by XPS and SEXAFS/NEXAFS on the deposition of K on HOPG at 298 K it appears that potassium intercalates through the graphite layers. This intercalation produces the expansion of the interlayer distance ($d = 5.34 \text{ \AA}$) and the rearrangement of the layers into an AA geometry. Simultaneously, there is an extensive transfer of charge from the potassium atoms to the layers. These conclusions agree with previous results by LEED of Ignatiev et al. [4] on the site geometry of intercalated potassium and with the transfer of charge to the layers estimated by angle-resolved photoemission in previous papers of Hughes et al. [6–8] as one electron charge per K atom.

Partial oxidation of potassium and incorporation of oxygen into the system occurs by adsorption of O_2 at 298 K. Our XPS results have shown that under these conditions only part of the charge initially transferred from K to the graphite layers is back transferred to the oxygen.

Activation of the adsorption process by extra dosing of oxygen at 373 K leads to an additional incorporation of oxygen into the system.

The comparative analysis of the XPS and NEXAFS/SEXAFS spectra reveals that adsorption of oxygen induces a partial segregation of potassium to the surface where it becomes oxidized and forms a potassium oxide overlayer (likely to be K_2O_2) in which the K–O bonds are parallel to the surface of the substrate. The segregation can be activated thermally, so that at 373 K 45% of the atoms initially intercalated within the graphite layers segregate to the surface.

Acknowledgements

We thank the TMR program of the EU that enabled the measurements at the Daresbury synchrotron. The financial support of the DG CYT (project n. PB93-0183) is also acknowledged.

Appendix A

The EXAFS $\chi(k)$ function for a non-isotropic system with Gaussian disorder is given by [37]

$$\chi(k) = - \sum_i N_i^* A_i^*(k) \sin[2kR_i + \phi^i(k)], \quad (\text{A.1})$$

where A_i^* is the amplitude parameter, the index i labels atoms of the same atomic number located at the same distance R_i from the absorbing atom, the term $\phi^i(k)$ is the total phase shift and N_i^* is the effective coordination number that is given by

$$N_i^* = 3 \sum_{j=1}^{N_i} \cos^2 \alpha_{ij}, \quad (\text{A.2})$$

where α_{ij} is the angle between the electric field vector E at the central atom site and the vector r_{ij} from the central atom to the j th atom in the i th shell.

For a six-fold hollow site it can be shown that

$$\sum_{i=1}^6 \cos^2 \alpha_{ij} = 6 \cos^2 \beta \cos^2 \theta + 3 \sin^2 \theta \sin^2 \beta, \quad (\text{A.3})$$

where θ is the angle between the E vector and the surface normal and β is the angle between the adsorbate–substrate internuclear axis and the surface normal.

Taking into account the C–C distance in graphite (1.417 Å) and the distance C–K obtained by fitting in our experiment (3.026 Å) (see Table 2), it can be calculated that $\beta = 27.92^\circ$. Then, from Eq. (A3) the effective coordination numbers $N_i^*(\theta)$ for several incidences can be evaluated as shown in Table 3 for an atomic arrangement where the adsorbing atom is located within two hexagons

Table 3
 N_i^* values calculated for a double six-fold hollow site at several incidences angles

Incidence angle (θ) (degrees)	N_i^*
10	27.33
30	22.04
70	6.78
90	3.96

(i.e. $N_i = 12$). From this table the theoretical ratio N_{30}/N_{70} has a value of 3.25

References

- [1] H.P. Bonzel, A.M. Bradshaw and G. Ertl, Eds., *Physics and Chemistry of Alkali Metal Adsorption*, Materials Science Monograph 57 (Elsevier Amsterdam, 1989).
- [2] P.J. Benning, F. Stepniak, D.M. Poirier, J.L. Martins and J.H. Weaver, *Phys. Rev. B* 47 (1993) 13843.
- [3] Z.P. Hu, N.J. Wu and A. Ignatiev, *Phys. Rev. B* 33 (1986) 7683.
- [4] N.J. Wu and A. Ignatiev, *Phys. Rev. B* 28 (1983) 7288.
- [5] Z.P. Hu and A. Ignatiev, *Phys. Rev. B* 30 (1984) 4856.
- [6] M.T. Johnson, H.I. Starnberg and H.P. Hughes, *Surf. Sci.* 178 (1986) 290.
- [7] A.R. Law, M.T. Johnson and H.P. Hughes, *Surf. Sci.* 152/153 (1985) 284.
- [8] M.T. Johnson, H.I. Starnberg and H.P. Hughes, *Solid State Commun.* 57 (1986) 545.
- [9] S. Raaen, *Phys. Rev. B* 44 (1991) 3373.
- [10] R.M. Hock and R.E. Palmer, *Surf. Sci.* 284 (1993) 349.
- [11] Z.Y. Li, K.M. Hock and R.E. Palmer, *Phys. Rev. Lett.* 67 (1991) 1562.
- [12] J. Cui, J.D. White, R.D. Diehl, J.F. Annett and M.W. Cole, *Surf. Sci.* 279 (1992) 149.
- [13] J. Cui, J.D. White and R.D. Diehl, *Surf. Sci.* 293 (1993) L841.
- [14] D.V. Chakarov, P. Sjövall and B. Kasemo, *J. Phys. Condens. Matter* 5 (1993) 2903.
- [15] P. Sjövall and B. Kasemo, *J. Chem. Phys.* 98 (1993) 5932.
- [16] H. Shioyama, M. Crespin, A. Sern, R. Setton, D. Bonnin and F. Beguin, *Carbon* 31 (1993) 223.
- [17] V. Codazzi, G. Loupiaz, S. Rabii, L. Elansari, D. Guerard and I. Ascone, *J. Solid State Chem.* 94 (1991) 79.
- [18] S.L. Molodtsov, C. Casado, M.E. Davila, M. Moreno, F. Soria, M.C. Asensio, *J. Phys. Condens. Matter* 6 (1994) 925.
- [19] M. Kunpfer, D.M. Poirier and J.H. Weaver, *Phys. Rev. B* 49 (1994) 8464.
- [20] M. Posternak, A. Baldereschi, A.J. Freeman, E. Winner and M. Weinert, *Phys. Rev. Lett.* 50 (1983) 761.
- [21] H. Ishida and R.E. Palmer, *Phys. Rev. B* 46 (1992) 15484.
- [22] F. Ancilotto and F. Toigo, *Phys. Rev. B* 47 (1993) 13713.
- [23] T.R. Ohno, C. Gu, J.H. Weaver, L.P.F. Chibante and R.E. Smalley, *Phys. Rev. B* 47 (1993) 13848.
- [24] Z.P. Hu, N.J. Wu and A. Ignatiev, *Surf. Sci.* 177 (1986) 2956.
- [25] M. Vayer-Besançon, B. Rousseau and H. Estrade-Szwarckopf, *Surf. Sci.* 318 (1994) 169.
- [26] D. Bonnin, P. Kaiser, C. Fretigny and J. Desbarres, in *Structures Fines d'Absorption des Rayons X en Chimie*,

- Vol 3, Logiciels d'analyse EXAFS, Eds. H. Dexpert, A. Michalowicz and M. Verdaguer (Orsay, 1989).
- [27] J.J. Rehr, J. Mustre de Leon, S.I. Zabinsky and R.C. Albers, *J. Am. Chem. Soc.* 113 (1991) 5135.
- [28] B. Lamontagne, F. Semond and D. Roy, *J. Electron Spectrosc. Relat. Phenom.* 73 (1995) 81.
- [29] B. Rousseau and H. Estrade-Szwarckopf, *Solid State Commun.* 88 (1993) 1.
- [30] W. Kuch, M. Schulze, W. Schnurnberger and K. Bolwin, *Surf. Sci.* 287/288 (1993) 600.
- [31] G. Pirng, H.P. Bonzel and G. Broden, *Surf. Sci.* 122, (1982) 1.
- [32] S. Donian and M. Sunjic, *J. Phys. C, Solid State Phys.* 3 (1970) 285.
- [33] P.E. Batson, *Phys. Rev. B* 48 (1993) 2608.
- [34] N. Okuyama, M. Yamazaki, K. Tomita and H. Yasunaga, *Jpn. J. Appl. Phys.* 25 (1986).
- [35] J. Jupille, P. Dolle and M. Besancon, *Surf. Sci.* 260 (1992) 271.
- [36] B. Lamontagne, F. Semond and D. Roy, *Surf. Sci.* 327 (1995) 371.
- [37] J. Stöhr, in: *X-ray Absorption: Principles, Applications, Techniques of EXAFS, SEXAFS and XANES*, Eds. D.C. Koningsberger and R. Prins (John Wiley and Sons, New York, 1988) pp. 482–487.

Synthesis and crystal structure of Al_3BC , the first boridecarbide of aluminium

Falko D. Meyer, Harald Hillebrecht*

Institut für Anorganische und Analytische Chemie, and Freiburger Materialforschungszentrum FMF, Albertstr. 21, 79104 Freiburg, Germany

Received 14 August 1996

Abstract

Single crystals of the aluminium-rich boridecarbide Al_3BC with isolated boron and carbon are synthesized from the elements. The crystal structure can be described as a closest packing of Al (sequence ABACBC) with alternating layers of edge-sharing BAI_6 octahedra and trigonal bipyramids CAI_3 , linked by common corners. Al_3BC plays an important role in the processing of $\text{B}_4\text{C}/\text{Al}$ cermets.

Keywords: Boridecarbide of aluminium; Synthesis; Crystal structure; $\text{B}_4\text{C}/\text{Al}$ cermets

1. Introduction

Aluminium rich (Al-rich) phases of the system Al/B/C have been the topic of several recent investigations, since cermets and composite materials based on boroncarbide B_4C and Al became promising candidates as ceramic materials of high hardness and toughness in lightweight structures [1–13]. Similar to WC/Co cermets, B_4C is responsible for the hardness and Al acts as a metallic binder. If carbon fibres are used in an Al-matrix the damage by formation of Al_4C_3 can be suppressed by coating the fibres with boroncarbide [6,7]. $\text{B}_4\text{C}/\text{Al}$ cermets and ceramics offer several advantages. Besides the low density ($\rho \approx 2.5 \text{ g/cm}^3$) the high reactivity of Al allows sintering of green bodies without the application of pressure already at moderate temperatures. Furthermore the microstructure of the material can be modified by heating after the densification process (postdensification heat treatment, reactive “tailorable” ceramics). Finally dense materials are easier to achieve by sintering in the presence of a liquid phase [14]. In order to understand the reactivity of $\text{B}_4\text{C}/\text{Al}$ cermets, investigations on Al-rich compounds are of fundamental interest.

An Al-rich compound in the system Al/B/C was first reported in 1985 by Halverson et al. [1] and described as a metastable compound, but neither was a characterization done nor a detailed composition given. In later publications compositions between Al_4BC and $\text{Al}_{2.6}\text{B}_{1.8}\text{C}$ were proposed [2–5]. According to X-ray investigations on

powder samples Viala et al. [3] gave the composition Al_3BC and a hexagonal unit cell with $a = 3.491(2) \text{ \AA}$ and $c = 11.541(4) \text{ \AA}$, but the crystal structure was not determined. Therefore, there are still some open questions concerning conditions of formation, composition, and crystal structure of this Al-rich phase.

In the course of our investigations on ternary compounds of the system Al/B/C we recently have synthesized and determined the structure and properties of Al_3BC_3 , the first carbidecarbaborate of aluminium [15]. Now we report on synthesis, characterization, and crystal structure of the boridecarbide Al_3BC .

2. Synthesis

For the synthesis of Al_3BC the elements Al, B, and C were mixed in the molar ratio 8:1:1, pressed into pellets, and heated in a corundum crucible under an atmosphere of argon up to 850°C for 160 h. The crucible and sample were cooled at 150°C/h to room temperature. A metallic regulus was obtained. Under the microscope black-bluish hexagonal platelets with dimensions up to $1 \times 1 \times 0.05 \text{ mm}$ were visible grown from the solidified melt. X-ray powder diagrams showed, besides Al_3BC and excess Al, the compounds Al_4C_3 and AlB_2 . Attempts to isolate single crystals of Al_3BC by removing aluminium with dil. HCl failed because Al_3BC is attacked. Therefore single crystals of Al_3BC were hand-picked under the microscope for further investigations. As an aim of investigations currently in progress we are searching for more suitable methods

*Corresponding author. Fax: +49 761 203 6012.

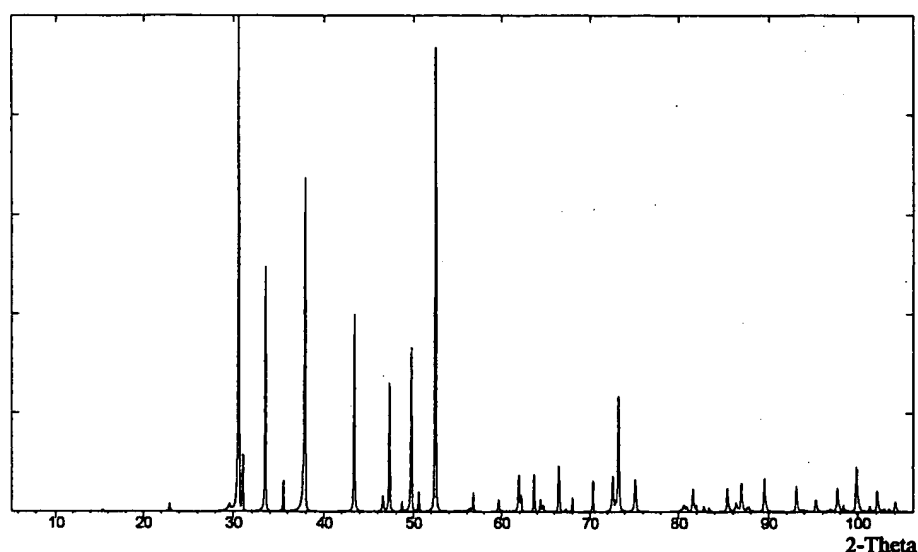
Fig. 1. X-ray powder diagram of Al_3BC ($\text{Cu-K}_{\alpha 1}$, PSD).

Table 1

X-ray powder diagram of Al_3BC (Cu-radiation, Ge-monochromator, PSD, 12 h). Refined lattice constants are $a=3.4875(3)$ Å, $c=11.5324(11)$ Å. Intensities are calculated from single crystal data

<i>h</i>	<i>k</i>	<i>l</i>	$2\theta_{\text{obs.}}$	$2\theta_{\text{calc.}}$	$d_{\text{obs.}}$	$I_{\text{obs.}}$	$I_{\text{calc.}}$	$I_{\text{publ.}}$ [4]
0	0	2	15.33	15.35	5.775	1.1	0.6	-
1	0	0	29.56	29.55	3.020	1.4	0.6	5
1	0	1	30.58	30.57	2.921	100	95.5	100
0	0	4	30.99	30.99	2.883	14.7	8.8	17
1	0	2	33.47	33.46	2.675	49.5	62.7	61
1	0	3	37.84	37.85	2.375	65.5	78.0	76
1	0	4	43.35	43.35	2.085	39.6	45.0	51
0	0	6	47.25	47.25	1.9221	25.6	28.1	30
1	0	5	49.70	49.69	1.8331	32.4	40.5	37
1	1	0	52.43	52.43	1.7438	92.1	100	69
1	0	6	56.73	56.72	1.6213	3.6	5.2	6
2	0	1	61.92	61.92	1.4973	7.2	10.1	10
1	1	4	62.19	62.16	1.4915	3.2	5.1	-
2	0	2	63.64	63.64	1.4609	7.5	11.5	10
1	0	7	64.36	64.35	1.4463	2.6	3.3	-
2	0	3	66.47	66.46	1.4055	9.4	15.0	13
2	0	4	70.32	70.31	1.3376	5.7	10.4	10
1	0	8	72.77	72.78	1.2996	5.2	9.7	5
1	1	6	73.39	73.39	1.2901	33.5	39.8	30
2	0	5	75.14	75.13	1.2633	6.4	9.8	10
1	0	9	81.72	81.71	1.1784	5.0	7.3	4
2	1	1	85.38	85.38	1.1361	4.6	6.2	-
2	1	2	86.92	86.92	1.1198	5.0	7.5	-
1	1	8	87.73	87.77	1.1116	0.6	1.1	-
2	1	3	89.48	89.48	1.0943	6.4	9.7	-
2	1	4	93.05	93.06	1.0615	5.3	7.7	-
2	0	8	95.24	95.24	1.0428	2.2	3.5	-
2	1	5	97.68	97.68	1.0231	4.8	7.0	-
3	0	0	99.83	99.83	1.0068	8.6	10.1	-
1	0	11	102.10	102.09	0.9905	4.2	5.1	-
2	1	6	103.39	103.40	0.9816	0.7	1.0	-
2	0	9	104.07	104.06	0.9770	2.0	2.6	-

of separation to get single phase samples of Al_3BC . The X-ray powder diagram in Fig. 1 results from some selected single crystals. All observed reflections with $I>5\%$ are listed in Table 1 and could be indexed with the hexagonal subcell. Weaker lines correspond to reflections from the superstructure as described by Gonzales et al. [4] or result from the by-products aluminium and Al_4C_3 . The d -values and intensities are in good agreement with published data and calculated values, based on the structural data of the subcell (see below). Minor deviations may result from orientation effects. Electron probe microanalysis with a wavelength-dispersive detector (Cameca SX100) confirmed the composition (ratio $\text{Al}:\text{B}:\text{C}=2.5:1:1$) and the absence of other elements.

3. Structure analysis

A fragment of a black-bluish hexagonal platelet was isolated from the regulus. Single crystal photographs taken with a Weissenberg camera (Cu-radiation) confirmed the hexagonal cell with $a=3.48$ Å and $c=11.52$ Å as found by Viala et al. [3] in the course of X-ray investigations on powders. On overexposed films additional superstructure reflections were visible. They require enlargement of the lattice constant a by a factor of $\sqrt{3}$. This kind of superstructure was already mentioned by Gonzales et al. [4] in connection with X-ray powder patterns and electron diffraction. The subsequent investigation with the four circle diffractometer initially reveals the hexagonal subcell ($a=3.4840(7)$ Å, $c=11.5202(18)$ Å) and after transformation in the course of the data collection the superstructure ($a'=6.0345(12)$ Å) as well. A detailed solution of the

Table 2
Crystal data and refinement of Al_3BC

Formula weight	103.76
Crystal system	hexagonal (subcell)
Space group	$\text{P6}_3/\text{mmc}$ (subcell)
a (Å)	3.4840(7)
c (Å)	11.5202(18)
V (Å ³)	121.10(4)
Z	2
d_{calc} (g/cm ³)	2.846
Radiation	MoK_α
μ (cm ⁻¹)	11.6
Crystal size (mm)	0.2×0.2×0.01
Temperature (°C)	20
Data coll. range	$\pm h, \pm k, l$
θ -range (°)	30
Scan method	$\omega/2\theta$
No. of refl. measured	675
No. of refl. observed	598
No. of refl. used	80 with $I > 0$
No. of variables	12
Absorption corr.	none
Weighting scheme	$w = 1/[\sigma^2(F_o^2) + (0.0067P)^2 + 0.07P]$ with $P = (F_o^2 + 2F_c^2)/3$
Extinction coeff.	0.127(26)
$\Delta\rho_{\text{max}}/\Delta\rho_{\text{min}}$ (e/Å ³)	+0.34/-0.28
$R_1(\text{F})$, 76 Refl	0.0173, all: 0.0291
$wR_2(I)$	0.0385, all: 0.0747
GooF	1.270

superstructure problem is a topic of further investigations and is planned to be finished in connection with a very similar problem of Al_3BC_3 [15]. Therefore the results presented in this work refer to the subcell.

Intensities of 675 reflections were collected by measuring half the Ewald sphere. In agreement with the results from film methods no deviations from Laue group 6/mmm could be detected. After averaging in 6/mmm a data set of 92 independent reflections was received. The reflection condition hkl with $l=2n$ led to the space groups $\text{P6}_3/\text{mmc}$, $\text{P6}_3\text{mc}$, and $\text{P6}_3\text{c}$. Following the results for Al_3BC_3 (subcell: space group $\text{P6}_3/\text{mmc}$) we started the structure solution in $\text{P6}_3/\text{mmc}$. Via Patterson methods (SHELXS86 [16]) we obtained a model that could be refined ($wR_2(I) = 0.32$; $R_1(\text{F}) = 0.12$). Difference Fourier syntheses and anisotropic refinements showed that one Al atom (Al2) occupies not the site 2b at 0 0 1/4, but seems to be disordered in the z -direction. Because the disorder is probably not dynamic, we suppose a static distortion, leading to the formation of the superstructure and a complex twinning, simulating the disorder of Al2. In the

Table 4
Selected distances and angles of Al_3BC

Distances (Å)		Angles (°)	
Al1–C	2.002(1)	C–Al1–B	113.57(2)
–B	2.195(1)	3× B–Al1–B	105.07(2)
–Al1	2.670(1)	3× Al1–Al1–Al1	81.45(2)
–Al2	2.677(1)	3× Al1–Al1–Al2	98.67(2)
Al2–C	2.025(1)	3× C–Al2–C	118.66(2)
–Al1	2.676(1)	3× C–Al2–Al1	116.76(2)
–Al1	3.048(1)	3× Al1–Al2–Al1	81.21(4)
...Al2'	0.473(3)		
		Al1–B–Al1	105.07(2)
B–Al1	2.195(1)	6× Al1–B–Al1	74.93(2)
C–Al1	2.002(1)	2× Al1–C–Al2	96.70(4)
–Al2	2.025(1)	3× Al2–C–Al2	120.44(1)/118.65(2)

subcell the disorder cannot be resolved because of the high symmetry and the small unit cell. As a consequence of the distortion there are also unequal values of U_{11}/U_{33} for Al1 and B. Based on 80 reflections and 12 variables the final refinement with disordered Al2 led to R -values of $wR_2(I) = 0.0385$ and $R_1(\text{F}) = 0.0173$ (SHELXL92 [17]). Refinements

Table 3
Coordinates and displacement parameters (in Å²) of Al_3BC

Atom	Site	x	y	z	U_{eq}	$U_{11} = U_{22}$	U_{33}
Al1	4f	1/3	2/3	0.07621(6)	0.0079(3)	0.0106(3)	0.0025(4)
Al2	4e*	0	0	0.27052(12)	0.0068(5)	0.0042(4)	0.0120(14)
B	2a	0	0	0	0.0145(9)	0.0025(9)	0.0386(38)
C	2d	2/3	1/3	3/4	0.0043(6)	0.0044(8)	0.0041(12)

* Refined as disordered with site occupation factor 1/6.

with free site occupation factors showed no significant deviation from full occupation. Table 2 contains further details of the structure determination, Table 3 the positional and displacement parameters, and Table 4 selected distances and angles. Additional data of the structure analysis are available from the Fachinformationszentrum Karlsruhe 76344 Eggenstein–Leopoldshafen by quoting the depository number CSD-380116, the names of the authors, and the journal citation.

4. Description of the structure and discussion

The most simple description of the crystal structure of Al_3BC is a closest packing of Al atoms with a layer sequence ABACBC. Isolated boron atoms are placed in all octahedral voids between the layers A and C while isolated C atoms occupy half of the trigonal voids in the layers B (Fig. 2). This leads to a pronounced two dimensional character because in that way layers of edge sharing Al_6B octahedra, similar to layer structures of the CdI_2 type, alternate with layers of trigonal bipyramidal Al_3C polyhedra linked by common corners. Both types of layers are connected via Al atoms (Al1). As a result from the occupation of voids by B and C the c/a ratio of 3.30 deviates considerably from an idealized value of $2\sqrt{6} \approx 4.90$. From the Al–Al distances of metallic aluminium values of $a = 2.863 \text{ \AA}$ and $c = 14.025 \text{ \AA}$ are expected, i.e., the expansion of the lattice constant a respectively the compression of c amounts to ca. 20% in both cases.

The topological principle described above is reflected in the coordinations of the individual atoms (Fig. 3). B is coordinated octahedrally by Al1. Al–B distances of $2.195(1) \text{ \AA}$ correspond to the sum of the atomic radii and are comparable to those found for other borides of Al. The B–Al–B angles of 75° and 105° demonstrate the consider-

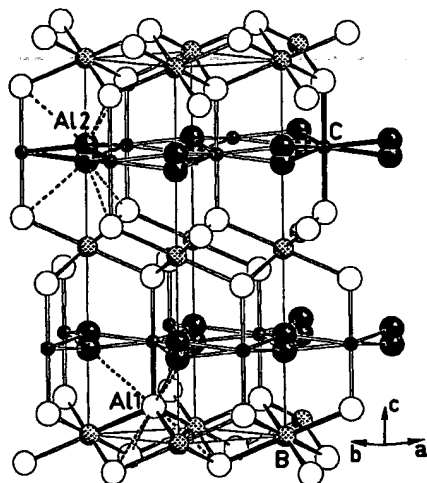


Fig. 2. Crystal structure of Al_3BC .

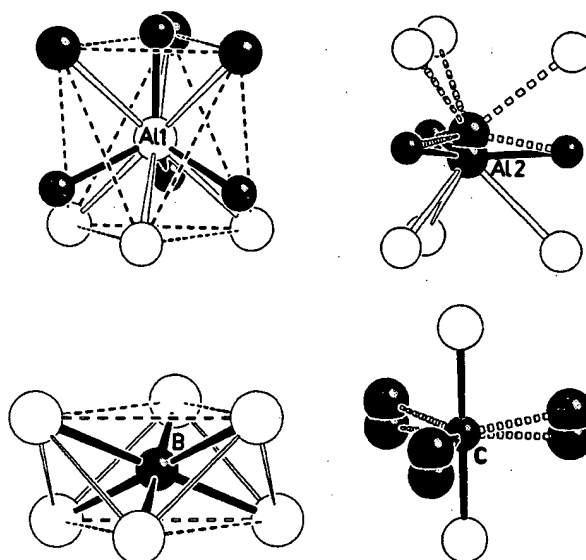


Fig. 3. Coordination polyhedra in Al_3BC .

able distortion of the BAl_6 octahedra. Similar to many other carbides of aluminium (i.e. Al_4C_3 [18], $\text{Al}_5\text{C}_3\text{N}$ [19], Al_3BC_3 [15]) the isolated C atoms are coordinated trigonally bipyramidally with nearly equal Al–C distances of $2.002(1) \text{ \AA}$ and $2.025(1) \text{ \AA}$.

Al1 is 10-fold coordinated by 6 Al, 3 B, and 1 C atom. Boron and carbon form a tetrahedron with one Al–C distance of $2.025(1) \text{ \AA}$ and three Al–B distances of $2.195(1) \text{ \AA}$. The 6 Al atoms build up an elongated octahedron with two triangles of Al1 respectively Al2. The B_3C tetrahedron is orientated in such a way that carbon lies above the Al2 triangle and boron above the edges of the Al1 triangle.

The coordination of Al2 in an undistorted structure without disorder would consist of three trigonal planar C atoms (Al–C: 2.00 \AA) on the edges of a trigonal prism built up by 6 Al1 (Al1–Al2: 2.832 \AA). This kind of aluminium coordination is unstable against distortions. In carbides $\text{Al}_5\text{C}_3\text{N}$ [19,20], Al_4SiC_4 [20], $\text{Zr}_3\text{Al}_3\text{C}_5$ [21], $\text{U}_2\text{Al}_3\text{C}_4$ [22], YbAl_3C_3 [23], and Al_3BC_3 [15] the Al atom with a trigonal bipyramidal coordination is not exactly in the center of the polyhedron. It is shifted ca. $0.2\text{--}0.3 \text{ \AA}$ towards one tip of the bipyramid and occurs in that way in a distorted tetrahedral coordination with nearly equal Al–C distances. In the case of Al_3BC a stabilization is achieved by a movement of Al2 towards one of the Al1 triangles and shortening the Al1–Al2 distance to $2.676(1) \text{ \AA}$. Al–Al distances between 2.6 and 2.7 \AA are found in many aluminium alloys [24], so a binding (metallic) interaction can be assumed. This symmetry reduction can be simulated for the subcell by a disorder of Al2 in the c direction, leading to a displacement from the center of about 0.24 \AA . The displacement parameters of Al1 and B

indicate that the formation of the superstructure causes shifts for these atoms, too.

The crystal structure analysis of Al_3BC confirms the composition as it was first given by Viala et al. [3]. There are isolated carbon atoms besides isolated boron and Al_3BC can be regarded as a real boridecarbide. Together with the well known Mo_2BC [25], Al_3BC represents the only examples of this class of compounds. Although many ternary compounds M/B/C are known for alkali, alkali earth, and rare earth metals (i.e. LiBC [26], MgB_2C_2 [27], CaB_2C_2 [28], Sc_2BC_2 [29], ScB_2C [30], LaB_2C_2 [28]) they all contain B–C bonds.

The crystal structure of Al_3BC is similar to Al_4C_3 [18,20]. In Al_4C_3 there are layers of edge sharing octahedra CaI_6 (composition Al_2C) instead of BaI_6 octahedra. These layers alternate not with single layers of trigonal CaI_3 groups but with double layers (composition Al_2C_2), leading to edge and corner sharing double layers of trigonal bipyramids CaI_5 . According to the stacking sequence ABABCACABCBC of aluminium a rhombohedral unit cell is realized. So the differences are an additional layer AlC, a modified layer sequence and the boron/carbon substitution.

As indicated by the stoichiometry Al_3BC shows a close relationship to Al_3BC_3 [15]. Just removing the C atoms of the CBC groups in Al_3BC_3 gives the structure of Al_3BC . In contrast to the carbidecarbaborate Al_3BC_3 with a clearly ionic character Al_3BC seems to be more metallic. With the assumption of C^{3-} anions and Al^{3+} cations there remain five electrons for the boron and the existence of the anion B^{5-} is very unlikely. Therefore we expect delocalized electrons and metallic behaviour. The result of this very simple counting of electrons is supported by colour (black-bluish), chemical behaviour (reaction with dil. HCl), and the structural features (short distances Al1–Al2) of Al_3BC . Electric conductivity measurements will be done as soon as single phase samples are accessible in sufficient quantities.

The organization of the crystal structure of Al_3BC would explain variations of the composition as mentioned by Pyzik and Beaman [5] and the additional lines of the X-ray powder diagram (Viala et al. [3]). A higher Al content (" Al_4BC ") results when additional layers of Al are inserted between the layers of Al1 and Al2 into the closest packing without changing the structure in principle. Additional boron content (" $\text{Al}_3\text{B}_{1.2}\text{C}$ ") may occur by additional layers of AlB_2 . In connection with these possible ways of changing the stoichiometry it should be mentioned that in the course of our investigations there were no signs of deviations from the composition Al_3BC .

Acknowledgments

The authors wish to thank Prof. G. Thiele (Freiburg) for his generous support of our work and the Deutsche

Forschungsgemeinschaft for funding this research (Hi 632/1-1).

References

- [1] D.C. Halverson, A.J. Pyzik and I.A. Aksay, *Ceram. Eng. Sci. Proc.*, 16 (1985) 736–744.
- [2] M. Sarikaya, T. Laoui, D.L. Milius and I.A. Aksay, *Proc. 45th Annu., Electron Microsc. Soc. Am.*, 1987, pp. 168–169.
- [3] J.C. Viala, G. Gonzales and J. Bioux, *Mater. Sci. Lett.*, 11 (1992) 711–714.
- [4] G. Gonzales, C. Esnouf and J.C. Viala, *Mater. Sci. Forum*, 126–128 (1993) 125–128.
- [5] A.J. Pyzik and D.R. Beaman, *J. Am. Ceram. Soc.*, 78 (1995) 305–312.
- [6] H. Vincent, B. Bonnetot, J. Bioux, H. Mourichoux and C. Vincent, *J. Phys.*, 50 (1989) 249.
- [7] M. Yang and V.D. Scott, *J. Mat. Sci.*, 26 (1991) 1609.
- [8] K. Wai, J.M. Yang and W.C. Harrigan, *Scripta Metall.*, 23 (1989) 1277.
- [9] J. Lecomte-Beckers and E. Diderichs, *ATB Metall.*, 27 (1987) 3.
- [10] D.C. Halverson, A.J. Pyzik, I.A. Aksay and W.E. Snowden, *J. Am. Ceram. Soc.*, 72 (1989) 775.
- [11] A.I. Kharlamov T.I. Duda and V.V. Fomenko, *AIP Conf. Proc.*, 231 (1991) 512.
- [12] R.J. Osof, P.H.A. Roebuck and D.P. Thompson, *Br. Ceram. Trans.*, 94 (1995) 25.
- [13] J.I. Jeong, B.M. Lim, J.H. Moon, J.H. Hong, J.S. Kang and Y.P. Lee, *J. Vac. Sci. Technol.*, A12 (1994) 873.
- [14] I.A. Aksay, C.E. Hoge and J.A. Paste, *J. Phys. Chem.*, 78 (1974) 1178.
- [15] H. Hillebrecht and F.D. Meyer, *Angew. Chem.*, 108 (1996) 2655; *Angew. Chem. Int. Ed. Engl.*, 35 (1996) 2499.
- [16] G. Sheldrick Programm SHELXS86, Göttingen, 1986.
- [17] G. Sheldrick Programm SHELXL92, Göttingen, 1993.
- [18] M. v. Stackelberg and E. Schorrenberg, *Z. Phys. Chem.*, 27 (1934) 37.
- [19] G.A. Jeffrey and M. Slaughter, *Acta Cryst.*, 16 (1963) 177.
- [20] F.D. Meyer and H. Hillebrecht, unpublished results.
- [21] Th.M. Gesing and W. Jeitschko, *15th European Crystallographic Meeting, Dresden, 1994*, Collected abstracts, p. 432.
- [22] Th.M. Gesing and W. Jeitschko, *Z. Kristallogr. Suppl.*, 7 (1993) 55.
- [23] Th.M. Gesing, R. Pöttgen, W. Jeitschko and U. Wortmann, *J. Alloys Compounds*, 186 (1992) 321.
- [24] W.B. Pearson, *The Crystal Chemistry and Physics of Metals and Alloys*, Wiley-Interscience, New York, 1972.
- [25] W. Jeitschko, H. Nowotny and F. Benesovsky, *Monatsh. Chem.*, 93 (1963) 565.
- [26] G. Mair, *Ph.D. Thesis*, University of Stuttgart, Germany, 1984; R. Ramirez, R. Nesper, H.-G. von Schnering and M.C. Böhm, *Z. Naturforsch.*, A42 (1987) 670.
- [27] M. Wörle and R. Nesper, *J. Alloys Compounds*, 216 (1994) 75.
- [28] J. Bauer and O. Bars, *Acta Cryst.*, B36 (1980) 1540.
- [29] J.-F. Halet, J.Y. Saillard and J. Bauer, *J. Less-Common Metals*, 158 (1990) 239.
- [30] J. Bauer, *J. Less-Common Metals*, 87 (1982) 45.

Density-functional based tight-binding calculations on zinc-blende type BC_2N -crystals

J. Widany ^a, W.S. Verwoerd ^a, Th. Frauenheim ^{b,*}

^a Department of Physics, University of South Africa, P.O. Box 392, Pretoria 0003, South Africa

^b Technische Universität, Institut für Physik, D-09107 Chemnitz, Germany

Received 5 August 1997; accepted 2 June 1998

Abstract

The ternary system B–C–N has attracted considerable attention in recent years, as a result of potentially interesting properties of the phases in this system. A non-self-consistent, ab initio based tight-binding molecular-dynamics method, has been used to investigate the stability, structural and electronic properties of BC_2N -crystals with zinc-blende structure. We investigate cubic crystals with different BN– C_2 stacking sequences in the [100] direction. The competition between structural stress and chemical bond strength can be seen as crucial for the formation of real ternary crystalline structures or a segregation into two cubic phases: diamond and *c*-BN. © 1998 Elsevier Science S.A. All rights reserved.

Keywords: Boron–carbon–nitride; Cubic BC_2N ; Phase-separation; Total energy calculations

1. Introduction

Compounds of boron and nitrogen with other elements, particularly the ternary boron–carbon–nitrogen system, possess technologically relevant properties. For example, it is expected that the conducting and intercalation properties of hexagonal B–C–N compounds may be intermediate between semi-metallic graphite and insulating hexagonal BN. On the other hand, cubic ternary phases should exhibit excellent mechanical qualities. The hardest known materials contain, exclusively, the elements boron, carbon and nitrogen. These elements provide the strongest three-dimensional network of covalent-bonds with very short bond lengths. The short bond length implies a high atom density and a high mass density comparable with diamond. A phase diagram for known B–C–N compounds is plotted in Fig. 1. Opposed to the diamond modification of carbon, there exists no hard materials formed by boron or nitrogen only, which is quite obvious from the fact that their electron configuration is improper for a totally filled sp^3 -orbital. While experimental work had success in their efforts towards a low-temperature, low-pressure growth of *c*-BN thin films over the last decade, the deposition of the super-

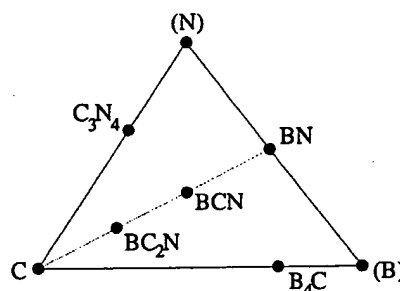


Fig. 1. B–C–N phase diagram.

hard hypothetical material C_3N_4 is still a challenge for experimental work.

2. Review of experimental and theoretical results

Numerous reports on the successful synthesis of ternary single-phase B–C–N compounds of certain composition (BCN , BC_2N , BC_4N) have been given in the literature over the last 25 years. The deposition methods used include various CVD-techniques [1,2] and solid phase pyrolysis [3,4]. However, as shown in Ref. [5], the evidence for the formation of the reported compounds provided by these studies is hardly exhaustive

* Corresponding author. Tel.: 0049 5251 60 2326;
Fax: +49 5251 60 3435; e-mail: frauenheim@phys.uni-paderborn.de

and is open to doubt. Thermal decomposition of pyridine–borane ($C_5H_5N-BH_3$) has been shown to be a suitable method for depositing graphite-like BC_2N and BC_4N films of high purity [6].

Several structure models have been proposed for graphite-like BC_2N [7], but the stability of these structures is not clear. Both random and ordered solid solutions of BN and C_2 should be possible, due to the isoelectronic and isostructural properties of BN and C_2 units. More recently, the focus of interest has shifted towards the synthesis of B–C–N nanotubes and boron doping of carbon nanotubes. Total energy calculations show that two-dimensional BC_2N tends to form strips or islands of pure BN and C [8]. The first evidence for such a phase separation was presented recently [9,10], where a substitution of C_2 by BN, as nanometre-size islands in graphitic structures, was found. Blase et al. [11] investigated theoretically the stability and electronic properties of composite $B_2C_2N_2$ nanotube heterojunctions, using both *ab initio* as well as semi-empirical approaches.

First attempts to deposit ternary zinc–blende structures were reported by Badzian in 1981 [12]. Recently, Nakano et al. published results of HTHP-synthesis of ternary phases starting from graphitic BC_2N [13,14]. A solvent-catalytic process using Co metal resulted in complete segregation, producing well-crystallized c -BN and diamond crystals, a few micrometers in dimension. Contrary to this, the treatment of graphitic BC_2N without any additive under HTHP-conditions ($T=2000$ – 2400 °C, $p=7.7$ GPa) led to several cubic phases. X-ray diffraction data strongly suggest segregative crystallization into c -BN, diamond and a cubic B–C–N structure. The stoichiometry of the latter phase was determined by Auger electron spectroscopy to a B:C:N ratio of 1:1.8:1.1. Attempts to grow cubic mixed phases by CVD processes have failed so far.

An elaborate study of the electronic structure of c -BN–diamond interfaces using linear muffin-tin-orbital (LMTO) and local density functional (LDF) methods, was presented by Lambrecht et al. [15]. The authors investigated $C_{2n}(BN)_n$ super-lattices ($n=1,3,5,7,9$) with the non-polar [110] interface. Generally, they found thermodynamic instability of the super-lattices with respect to segregation.

3. Method

3.1. Calculation of the total energy

To determine the total energy and the interatomic forces for a given set of atomic positions, we use a non-orthogonal tight-binding (TB) scheme. In contrast to most other TB methods, the Hamiltonian and overlap matrix elements are not obtained from a fit to an

experimental database, but derived from self-consistent local density approximation calculations. For details we refer the reader to a recent publication [17].

First, appropriate (pseudo)-atoms of each type are constructed by solving a modified atomic Kohn–Sham equation with an additional potential $(r/r_0)^2$ to the Perdew–Zunger LDA potential. This additional term, first introduced by Eschrig et al. [18], leads to a confinement of the atomic wave functions and, therefore, anticipates the main effect on the electron density in a bonded environment. In our case, the radius r_0 was chosen to be 2.8, 2.7 and 2.6 a_0 for B, C and N, respectively.

Second, the overlap and Hamiltonian matrix elements are calculated. Several contributions to the Hamiltonian matrix can be neglected. In fact, only two-centre elements are dealt with. The so-generated matrix elements depend only on the interatomic distance. This dependency has to be calculated only once for each possible pair of interaction.

It is well known that the total energy for a given set of coordinates $\{R_k\}$ can be approximated as a sum of the band structure energy (which is the sum of the occupied Kohn–Sham eigenvalues) and a sum of short-range repulsive pair-potentials:

$$E_{\text{tot}}(\{R_k\}) = \sum_i n_i \epsilon_i(\{R_k\}) + \sum_{k < l} V_{\text{rep}}(|R_l - R_k|). \quad (1)$$

For simple diatomic molecules this equation can be solved to give the repulsive potential for the related interaction pair, as the last sum reduces to only this term. One only has to determine the total energy versus interatomic distance from a self-consistent LDA calculation and the band structure energy from the already generated matrix elements. From the difference of both, one obtains the repulsive potential, which can be used generally for this combination of interacting atoms. Once this set of input data for the TB (Hamiltonian and overlap matrix, repulsive potential) is generated for each interaction pair, it can be used for various problems, e.g. the determination of equilibrium geometries, total energies, vibrational analysis for clusters, and molecules and solid-state modifications.

It has to be noted that the method is not self-consistent in charge density and, therefore, the charge transfers in ionic systems must be treated as approximate. There are no long-range Coulomb terms included in this model. However, the already published results of test calculations, considering clusters, molecules and crystalline phases, prove the accuracy of the potentials [17,19,20].

3.2. Generation of the structural models

There are different possibilities for the atomic arrangement within the cubic BC_2N crystal. The formation of

B–B and N–N bonds in a ternary is unlikely to occur, as they basically correspond to anti-site defects which have a large energy of formation. In the following, we will investigate (BN) C_2 stacking sequences in the [100] direction, regarding their structural and electronic properties. To evaluate the energetic stability of the ternary crystal compared with the formation of segregated pure diamond and *c*-BN phases, we consider models with variable thickness of the BN- and C_2 -layers. In Section 4 we write (BN) $_n$ (C_2) $_m$, with n specifying the number of layers within the stacking sequence. It has to be noted, that the cleavage in the [100] direction leads to the formation of two different polar interface regions in the crystal, containing B–C and N–C bonds, respectively. For large numbers of n this could lead to macroscopic electric fields and metallic character of the interfaces. The crystals are modelled as super cells with periodic extensions in all three dimensions. The super cells contain between 128 and 512 atoms, according to the different arrangement of the layers. In order to determine the energetically most stable configuration we vary the volume of the super cell. The atom positions in the super cells are geometrically optimized, using a conjugate gradient relaxation scheme.

4. Results for cubic BC_2N crystals

Structural and electronic properties of the various models will be discussed in this section. The cohesive energies of the BC_2N crystals, compared with that of diamond and *c*-BN, are displayed in Fig. 2. The energies are calculated with respect to the non-spin-polarized atoms, which has the effect of exaggerating the cohesive energies.

The given lattice parameter should be considered as a counterpart of the volume of the optimized super cells. The volume of the super cell defines an averaged bond length r_{avg} of the model. We define the lattice parameter as:

$$a = \frac{r_{avg}^* 4}{\sqrt{3}}. \quad (2)$$

The expression “lattice parameter” is not exact for the models with large n , but its usage allows a simple comparison of the geometrical and energetic properties of the models. It has to be noted that, for two models, the most stable structures are not derived by simple expansion of the cubic super cell. An additional expansion in the z -direction lowers the cohesive energy for the (BN) C_2 structure and the model with B–C–N–C stacking, named as BCNC in the following.

The properties and the cohesive energy of the structures with large n are determined by the two bulk structures, diamond and *c*-BN. The influence of the

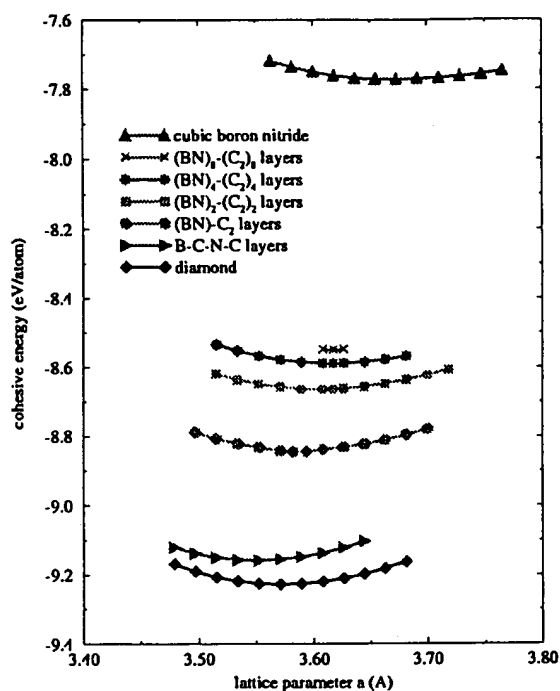


Fig. 2. Lattice parameter and cohesive energies of BC_2N -crystals with [100] stacking.

interfaces between the pure modifications should be small. The cohesive energy of this ternary structure is expected to converge to a value of:

$$E_{BC_2N} \rightarrow \frac{1}{2} (E_{diamond} + E_{c-BN}). \quad (3)$$

For the evaluation of the stability of ternary phases we have to estimate the formation energy of the BC_2N super-lattice:

$$E_f = E_{BC_2N} - \frac{1}{2} (E_{diamond} + E_{c-BN}). \quad (4)$$

The distortion of the lattice geometries of the pure modifications due to the lattice mismatch, have to be taken into account. However, the expansion of the diamond lattice and the contraction of the *c*-BN lattice to $a = 3.617 \text{ Å}$, decreases the cohesive energy only slightly by 0.01 eV per atom, respectively.

Generally, we derive negative values for E_f , indicating thermodynamic stability of the ternary phases with respect to phase separation. Moreover, the cohesive energy is lowered with decreasing values of n . The formation of a compound is found to be energetically clearly favoured with respect to the separation into individual bulk solids. In Table 1, the formation energies are compiled. In all evaluated models each of the two interface regions contains 32 atoms, therefore, the calcu-

Table 1
Formation energies of ternary $(\text{BN})_n(\text{C}_2)_n$ super-lattices

structure	E_f (eV/interface-unit cell)
BCNC	−0.659
$(\text{BN})\text{C}_2$	−0.340
$(\text{BN})_2(\text{C}_2)_2$	−0.165
$(\text{BN})_3(\text{C}_2)_3$	−0.115
$(\text{BN})_4(\text{C}_2)_4$	−0.089
$(\text{BN})_5(\text{C}_2)_5$	−0.074
$(\text{BN})_6(\text{C}_2)_6$	−0.063
$(\text{BN})_7(\text{C}_2)_7$	−0.056
$(\text{BN})_8(\text{C}_2)_8$	−0.050

lated formation energies per interface-unit cell are directly comparable.

These results are in contradiction to the work of Lambrecht et al. [15,16]. The authors found in their study of diamond c -BN [110] interfaces, positive values for the energy of formation of $(\text{BN})_n(\text{C}_2)_n$ super-lattices. No optimization of the atom positions took place in their calculations. We calculate the energy gain obtained by geometrical relaxation of the super cell to 0.025 eV per atom.

We want to carry out a simple comparison of the binding energies for single bonds between the different atom species, as calculated by the DF-TB method. From the crystalline modifications, we found 3.89 eV for the B–N bond (c -BN), 4.61 eV for the C–C bond (diamond), and 5.22 eV for the C–N bond (β - C_3N_4). A correspondent B–C value is hard to estimate, as a result of the lack of a crystalline modification, containing only B–C single bonds. Therefore, we construct a hypothetical cubic BC structure, analogous to c -BN. The calculated cohesive energy amounts to 4.1 eV for the B–C bonds. We find the formation of B–C and C–N single bonds energetically preferred to that of B–N bonds. The distortions of the lattice geometries in the interface regions are rather small. We conclude that the energy gain, obtained by the formation of B–C and C–N bonds, prevails the energy loss, as a result of the lattice deformations.

In the following, we will analyse the super-lattices in more detail, starting with structures with $n \geq 2$. These models can be considered as bulk material with isolated interfaces. In Fig. 3, the structure model of $(\text{BN})_4(\text{C}_2)_4$ is shown as an example. It is reasonable to expect that the lattice parameter, a , of a ternary hybrid will be intermediate between those of the two parent structures. The lattice parameter for the optimized structures is determined to be $a = 3.62 \text{ \AA}$, which matches the average over the diamond ($a = 3.57 \text{ \AA}$) and c -BN ($a = 3.67 \text{ \AA}$) values. The atom density of the structure amounts to $\rho = 3.42 \text{ g/cm}^3$.

The different lengths of the interface bonds cause distortions of the bonding geometries. The B–C interface

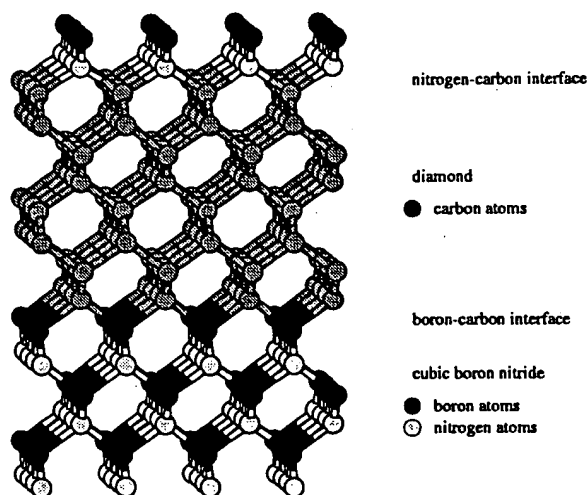


Fig. 3. Layered $(\text{BN})_4(\text{C}_2)_4$ -crystal.

bonds are obtained with bond lengths of 1.582 \AA , and the N–C bonds with 1.513 \AA . The mismatch of the bond lengths is compensated by alternating bond angles, leading to a local contraction (B–C interface) and expansion (N–C interface) of the structure in the z -direction. However, only the two nearest atomic layers of the c -BN and diamond sections are influenced by the distortions. The B–N bonds within the c -BN layer are found slightly contracted to 1.581 \AA , the C–C bonds in the bulk-like diamond layer are slightly expanded to 1.556 \AA .

To obtain some insight into the electronic properties of the structures, we evaluate the Mulliken charge distribution: The atoms in the c -BN and the diamond layer exhibit bulk-like behaviour. In the BN layer we find a charge transfer of $\pm 0.29 e$, similar to that of crystalline c -BN. The atoms in the diamond layer exhibit charge neutrality. Only the nearest atoms to the interface show slight deviations from these bulk-like values.

The boron atoms at the B–C interface are almost neutral, with a Mulliken charge of $+0.01 e$, the corresponding carbon atom is negatively charged by $-0.36 e$. The compensation of this charge is found in the N–C interface. There, the carbon atom shows a Mulliken charge of $+0.33 e$, while the according nitrogen is found with $+0.06 e$. Compared with the charges in the bulk material, we note a considerable charge transfer of approximately $0.65 e$ per interface atom between the interfaces. We determine an electron excess at the B–C interface and an according electron deficiency at the N–C interface.

The formation of polar interface layers with a large distance between them, leads to the question of whether their electronic behaviour can be described correctly without the introduction of long-range Coulomb interaction terms. For the model with $n = 4$, the distance

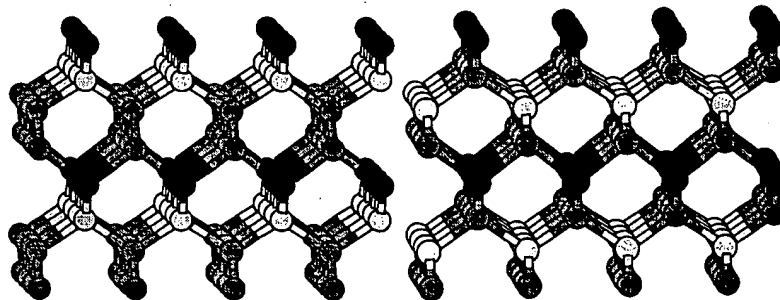


Fig. 4. Compound crystals with BC_2N stoichiometry: (a) $(BN)C_2$ -structure, and (b) BCNC-structure.

between the interface layers is approximately 7 Å. The interatomic potentials have already vanished within this distance. This means that our method does not describe properly the interaction between these interface layers. We should additionally take into account the electrostatic effects caused by the charged interfaces. The charge transfers could lead to metallic character of the interfaces, as already discussed in Ref. [15].

The $(BN)C_2$ structure, shown in Fig. 4a, already shows characteristics of a new compound. One part of the carbon atoms has two boron and two carbon neighbours, while the other part is bonded to two nitrogen and two carbon atoms, respectively. The geometrical optimization to find the super cell with the lowest cohesive energy, results in an averaged bond length $r_{xy} = 1.5501$ Å and an additional expansion in the z -direction by 1%. The density is found close to that for diamond, we calculate $\rho = 3.501$ g/cm³. The bond lengths are determined to 1.593 Å for B–N, 1.576 Å for B–C, 1.506 Å for N–C, and 1.549 Å for the C–C bonds, respectively. The charge distribution is similar to the model discussed above. The boron and nitrogen atoms are almost neutral with $-0.01 e$ and $+0.05 e$, respec-

tively. Between the carbon atoms, a charge transfer is obtained. We calculate a Mulliken charge of $-0.38 e$ for the carbon, attached to the nitrogen, and $+0.34 e$ for the carbon, attached to the boron, respectively. The charge transfers is a rather local effect, in contrast to the models with large values of n .

The $(BN)C_2$ structure can be seen as a special case, according to the fact that the [100] super-lattice is simultaneously a [110] super-lattice. The electronic band structure, displayed in Fig. 5a, is found to be in good agreement with the results shown in Ref. [15]. We determine a direct band gap at Γ of approximately 7.38 eV. It should be noted that the calculations are performed using a minimal basis set. Only the valence bands are properly described in this way, the description of the conducting bands requires the use of an extended basis set.

Finally, the BCNC model represents a completely different bonding structure. In this type of crystal no bulk-like C–C or B–N layers occur, the structure contains only B–C and C–N bonds, as shown in Fig. 4b. Therefore, the properties of this structure differ substantially from that of the other BC_2N models.

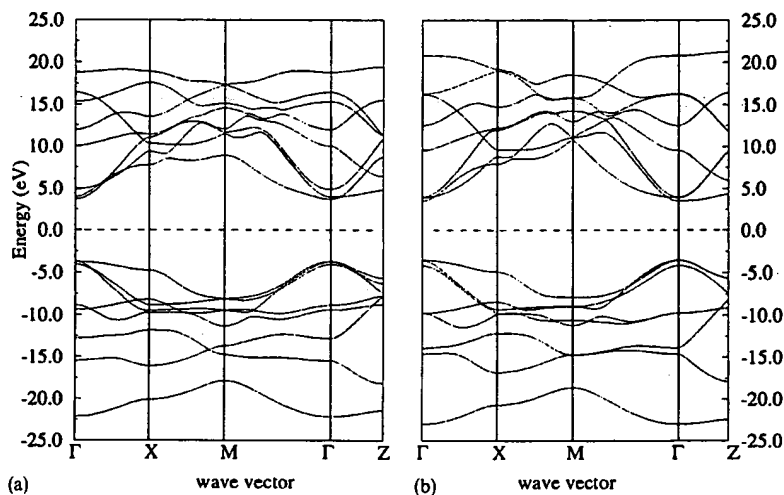


Fig. 5. Band structure of BC_2N compound crystals: (a) $(BN)C_2$ -structure, and (b) BCNC-structure.

We determine bond lengths of 1.578 Å and 1.505 Å for the B–C and C–N bonds, respectively. The formation of these short bonds leads to a very high atom density of 3.60 g/cm³ for the crystal. Owing to the different bond lengths, the formation of ideal tetrahedral bond angles of 109.4° is impossible. The B–C–B bond angles are clinched to 105.2°, while the N–C–N bond angles are stretched accordingly to 112.9°.

In contrast to the models considered above, we note a charge transfer from the boron to the nitrogen atoms. The Mulliken charges are determined to be $-0.33 e$ for the boron, $+0.45 e$ for the nitrogen, and $-0.06 e$ for the carbon atoms. The changes in the band structure, displayed in Fig. 5b, are less significant. We obtain a direct band gap of 6.88 eV at Γ .

The formation energy of -0.659 eV for the BCNC structure, indicates its high stability. Its cohesive energy is comparable with that of diamond. The energy gain obtained by forming this compound is remarkably higher than that obtained from the formation of individual bulk solids with separated interfaces.

5. Summary

We find the formation of a compound material to be energetically favourable with respect to the segregation into two “pure” crystals.

The interface region of super-lattices with higher values of n extends essentially over two layers on either side of the interface. A considerable charge transfer between the polar interfaces is found. We determine an electron excess at the B–C interface and an according electron deficiency at the N–C interface. The inclusion of a self-consistent treatment of the charges seems to be necessary to describe the long-range interaction between the interface regions.

The energy gain which is obtained by forming B–C and C–N bonds is higher than the energy loss due to the distortions of the bonding geometries at the interfaces. Congruously, the structure with the largest intermixing of the atom species, i.e. the highest amount of B–C and C–N bonds, is found to be most stable. According to the criteria discussed above, this structure is a possible candidate for a super-hard material: it exhibits a very high atom density, short bond lengths in a tetrahedral bonding arrangement, and high bonding energy.

It should be noted that our calculation concerns two-dimensional stackings only. The formation of three-dimensional crystallites in real HTHP-experiments leads, necessarily, to the generation of different interface structures, whose energetic behaviour is currently under investigation.

Acknowledgement

The author gratefully acknowledges financial support from the University of South Africa. Moreover, the work has been supported by the Deutsche Forschungsgemeinschaft. Special thanks to G. Jungnickel, TU Chemnitz, for allowing the use of the statix-program and for helpful discussions.

References

- [1] R.B. Kaner, J. Kouvetakis, C.E. Warble, M.L. Sattler, N. Bartlett, *Mater. Res. Bull.* 22 (1987) 399.
- [2] T.M. Besmann, *J. Am. Ceram. Soc.* 73 (1990) 2498.
- [3] J. Bill, M. Frieszlig, R. Riedel, *Eur. J. Solid State Inorg. Chem.* 29 (1992) 195.
- [4] M. Kawagushi, T. Kawashima, *J. Chem. Soc., Chem. Commun.* (1993) 1133.
- [5] T. Lundström, Y.G. Andreev, *Mater. Sci. Engng A209* (1996) 16.
- [6] R. Riedel, J. Bill, G. Passing, *Adv. Mater.* 3 (1991) 551.
- [7] A.Y. Liu, R.M. Wentzovitch, M.L. Cohen, *Phys. Rev. B39* (1989) 1760.
- [8] H. Nozaki, S. Itoh, *J. Phys. Chem. Solids* 57 (1996) 41.
- [9] O. Stephan, P.M. Ajayan, C. Colliex, Ph. Redlich, J.M. Lambert, P. Bernier, P. Lefin, *Science* 266 (1994) 1683.
- [10] Ph. Redlich, J. Loeffler, P.M. Ajayan, J. Bill, F. Aldinger, M. Rühle, *Chem. Phys. Lett.* 260 (1996) 465.
- [11] X. Blase, J.-C. Charlier, A. DeVita, R. Car, *Appl. Phys. Lett.* 70 (1997) 197.
- [12] A.R. Badzian, *Mater. Res. Bull.* 16 (1981) 1385.
- [13] S. Nakano, M. Akaishi, T. Sasaki, S. Yamaoka, *Chem. Mater.* 6 (1994) 2246.
- [14] S. Nakano, M. Akaishi, T. Sasaki, S. Yamaoka, *Mater. Sci. Engng A209* (1996) 26.
- [15] W.R.L. Lambrecht, B. Segall, *Phys. Rev. B40* (1989) 9909.
- [16] W.R.L. Lambrecht, B. Segall, *Phys. Rev. B47* (1993) 9289.
- [17] D. Porezag, Th. Frauenheim, Th. Köhler, G. Seifert, R. Kaschner, *Phys. Rev. B51* (1995) 12947.
- [18] H. Eschrig, *Optimized LCAO Method and the Electronic Structure of Extended Systems*, Akademie, Berlin, 1988.
- [19] J. Widany, Th. Frauenheim, Th. Köhler, M. Sternberg, D. Porezag, G. Jungnickel, G. Seifert, *Phys. Rev. B53* (1996) 4443.
- [20] J. Widany, F. Weich, Th. Köhler, D. Porezag, Th. Frauenheim, *Diamond Relat. Mater.* 5 (1996) 1031.

Anode materials for lithium ion batteries by oxidative treatment of common natural graphite

Y.P. Wu^{a,b,*}, C. Jiang^a, C. Wan^a, R. Holze^b

^a*Division of Chemical Engineering, INET, Tsinghua University, Beijing 102201, China*

^b*Technische Universität Chemnitz, Institut für Chemie, AG Elektrochemie, D-09107 Chemnitz, Germany*

Received 18 January 2002; received in revised form 17 May 2002; accepted 10 July 2002

Abstract

Modification of graphite has recently moved into the focus of the preparation of anode materials for lithium ion batteries. We report on an oxidative treatment by air and concentrated nitric acid solution to improve the electrochemical performance of a common natural graphite. Results from X-ray photoelectron spectroscopy (XPS), electron paramagnetic resonance (EPR), thermogravimetry (TG) and differential thermal analysis (DTA), high resolution electron microscopy (HREM), and measurements of the reversible electrochemical capacity suggest that the surface structure of natural graphite is changed and a fresh dense layer of oxides is formed. Structural imperfections are removed and the stability of the graphite structure is increased. These changes inhibit electrolyte decomposition, block intercalation of solvated lithium ions and prevent graphene planes from moving along the *a*-axis direction. In addition, nanochannels and micropores are introduced, and thus, lithium intercalation and deintercalation are favored and more sites are provided for lithium storage. Consequently, reversible capacity and cycling behavior of the modified natural graphite through the oxidation treatments is improved considerably. Since common natural graphite is low in cost, this method is promising for industrial application.

© 2003 Elsevier Science B.V. All rights reserved.

Keywords: Lithium ion batteries; Natural graphite; Oxidation; Anode materials

1. Introduction

Due to its many advantages over traditional rechargeable batteries, the development of lithium ion battery has been very rapid since its birth at the end of 1980s and in the early 1990s. So far, many anode materials such as amorphous carbon, tin com-

posite oxides, nitrides of lithium and transitional elements and novel alloys have been investigated, but graphitic carbon is still the dominating material on the market. With this background, modification of graphite became a recent focus in order to improve electrochemical performance and/or lower cost. For example, other kinds of carbonaceous materials were coated onto the surface of graphite such as pitch coke, pyrolytic carbons from pyrolysis of phenol-formaldehyde resin and from chemical vapor deposition [1–9]. Metals and metal oxides were deposited onto the surface of natural graphite such as silver, copper and

* Corresponding author. Technische Universität Chemnitz, Institut für Chemie, AG Elektrochemie, D-09107 Chemnitz, Germany. Fax: +49-371-531-1371.

E-mail addresses: wuyp99@hotmail.com (Y.P. Wu), rudolf.holze@chemie.tu-chemnitz.de (R. Holze).

its oxide, aluminum, and nickel [10–15], and the obtained composites showed a considerably improved electrochemical performance as anode materials. After coating with polymers such as gelatin and epoxy resin by dipping graphite in their solutions, the irreversible capacity in the first cycle decreased [16,17]. Graphite was also mildly oxidized with air, oxygen, carbon dioxide or ozone, or fluorinated by fluorine gas [1,18–23].

However, there are various species of graphitic carbons. Differences in source, treatment, and processing will result in striking differences in the surface and the body structure and a different electrochemical performance after oxidative treatment [18–23]. Recently, we investigated one kind of natural graphite from China, whose reversible capacity was low, about 250 mAh/g, and faded to 100 mAh/g within 10 cycles. It is much poorer in electrochemical properties than materials other researchers have used [18–23]. Nevertheless, after oxidative treatment with green chemicals such as solutions of H_2O_2 and $\text{Ce}(\text{SO}_4)_2$ [24], its electrochemical performance was much improved. This kind of natural graphite is common, and our results are different from those reported elsewhere [18–23]. We concluded that structural imperfections were removed by oxidative treatment [24]. However, these chemicals are expensive. In the present study, we report on a modification of natural graphite by oxidation with cheap substances like, e.g. air and nitric acid solution. Preliminary results show that its reversible capacity can be above 330 mAh/g, and cycling behavior is very good.

2. Experimental

The natural graphite used was from China (designated as D) with interlayer distance d_{002} 3.351 Å, crystal size L_c 120 Å, average particle size diameter 17 µm and carbon content >99%. Two ways were tried to oxidize it. The first one used air as an oxidant. Oxidation was performed at 550 °C in a tube furnace under air, and the obtained sample was marked OA. The other method used a concentrated nitric acid solution (63% HNO_3) as oxidant. The modification was carried out by dipping D in the solution under stirring at 60 °C followed by washing with water until the elute was neutral and

subsequent drying. The prepared product was marked ON.

X-ray photoelectron spectra (XPS) were obtained with an ES-300 spectrometer, and the relative contents of O and C at the surface of the natural graphite were calculated on the basis of their photoionization cross-sections and the integrals of their X-ray photoelectron intensities. Electron paramagnetic resonance (EPR) spectra were recorded on an EPR-200 spectrometer (BRUKER, Germany). Thermogravimetry and differential thermal analysis (TG-DTA) were performed with an instrument PCT-1 under air, the heating rate was 20 °C/min. High resolution electron micrographs (HREM) were recorded with a JEM-200CX microscope (JEOL, Japan) under vacuum. Samples were uniformly pre-dispersed on micro-nets with cavities of µm size.

Capacity and cycling behavior were tested according to the method described elsewhere [24], which used lithium foil as counter and reference electrode, 1 mol/l LiClO_4 solution in a mixture of EC/DEC (v/v=3:7) as the electrolyte and homemade porous PP film as the separator. The anode was prepared by pressing the mixture of natural graphite and 5 wt.% binder PVDF dissolved in N,N' -dimethyl formamide into pellets with a diameter of ca. 1 cm. After drying under vacuum at 120 °C over night, the anode pellets were put into an argon glove box and assembled into model cells. Electrochemical performance was measured galvanostatically at 0.2 mA with a CT2001A cell test instrument (Wuhan LAND Electronic, China), discharge (intercalation process) and charge (deintercalation process) voltages were ranged from 0.0 to 2.0 V versus Li^+/Li .

3. Results and discussions

It is well known that a lot of structural imperfections/defects such as sp^3 -hybridized carbon atoms, edge carbon atoms and carbon chains exist in graphite [24–27] especially in natural graphite owing to its incomplete graphitization during the natural formation process. These kinds of structures are prone to the attack by oxygen and chemical oxidants, and consequently, some of them may be removed by oxidation with air or the nitric acid solution. In addition, the surface structure of the

natural graphite D may be changed after the oxidation reactions.

XPS spectra of O_{1s} and C_{1s} in the samples D, OA and ON are shown in Figs. 1 and 2, and selected data are summarized in Table 1. In the case of oxygen atoms, four species are present, i.e. hydroxyl/phenolic group, ether oxygen, carboxylic oxygen in $-\text{COOR}$

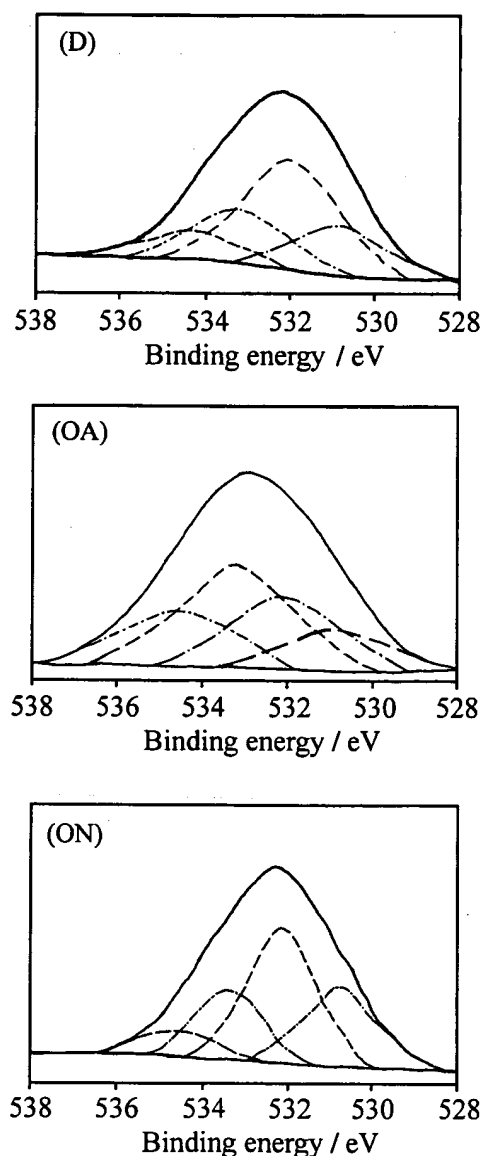


Fig. 1. XPS spectra of O_{1s} at the surface of natural graphite before (D) and after oxidation by air (OA) and nitric acid solution (ON).

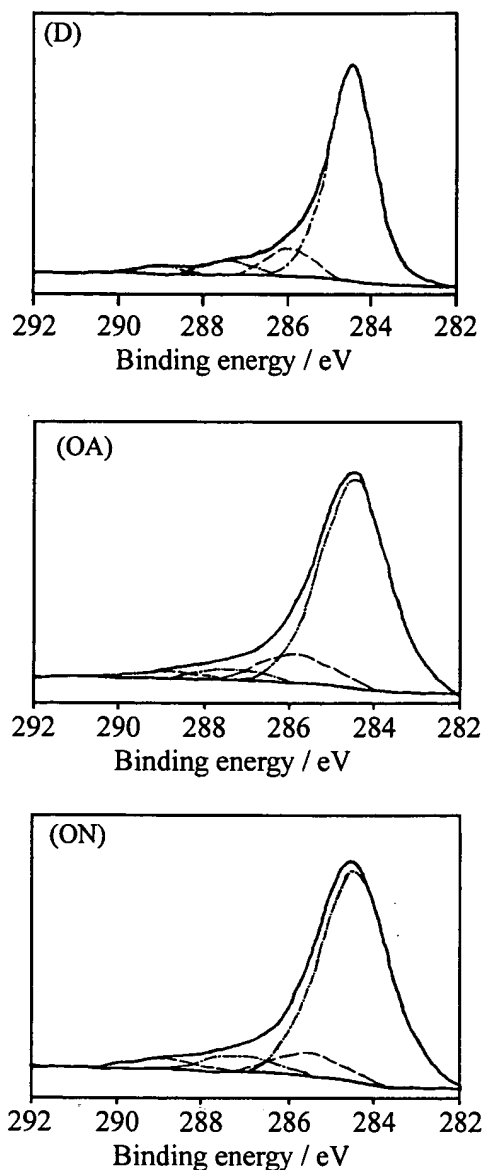


Fig. 2. XPS spectra of C_{1s} at the surface of natural graphite before (D) and after oxidation by air (OA) and nitric acid solution (ON).

($R=\text{H}$ and alkyl) and carbonyl oxygen in acetone/quinone, which correspond to binding energy peaks at 534.1, 533.2, 532.3 and 530.9 eV, respectively [24,28]. As to carbon atoms, four species are also present, i.e. carbonyl carbon in acetone/quinone, carboxylic carbon in $-\text{COOR}$ ($R=\text{H}$ and alkyl), ether/phenolic carbon in $\text{C}-\text{O}-\text{C}$ and $\text{C}-\text{OH}$, and carbon

Table 1

Selected results of the natural graphite before (D) and after oxidation by air (OA) and nitric acid solution (ON)

Sample	Oxidation treatment	Weight loss/%	Atomic ratio of O at the surface/%	Atomic ratio of C at the surface/%	Species and contents of oxygen atoms				Species and contents of carbon atoms			
					534.1 eV	533.2 eV	532.3 eV	530.9 eV	288.9 eV	287.2 eV	285.9 eV	284.4 eV
D	–	–	4.11	95.89	0.1268	0.2320	0.4526	0.1886	0.0299	0.0534	0.1029	0.8138
OA	Air, 500 °C	9.33	3.00	97.00	0.2080	0.4018	0.2538	0.1365	0.0275	0.0399	0.1255	0.8071
ON	Nitric acid, 60 °C	1.98	3.96	96.04	0.1006	0.2128	0.4188	0.2622	0.0438	0.0610	0.0902	0.8050

atoms in graphene planes, which correspond to peaks of binding energy at 288.9, 287.2, 285.9 and 284.4 eV, respectively [24,28].

Natural graphite chemi- and physisorbs oxygen-containing species like, e.g. water, oxygen and CO₂. Moreover, this kind of natural graphite was dipped in KOH solution before further treatment in order to remove minerals. Consequently, oxides were already present before oxidation. In the case of air oxidation, the relative contents of hydroxyl/phenolic group (534.1 eV), ether oxygen (533.2 eV) increased after the oxidation, which is consistent with the increase of the relative content of ether/phenolic carbon in C–O–C and C–OH (285.9 eV). In contrast, in the case of oxidation by the nitric acid solution, the relative contents of carbonyl oxygen in acetone/quinone (530.9 eV) increased, which is also consistent with the increase of the relative contents of carbonyl carbon in acetone/quinone (288.9 eV) and carboxylic carbon in –COOR (R=H and alkyl) (287.2 eV). In both cases, the oxygen content at the surface of graphite decreased after the oxidation from 4.11% to 3.00% (OA) and 3.96% (ON), respectively. The changes in the oxygen content and relative contents of each species of carbon and oxygen atoms are quite different from the data previously reported after oxidation with solutions of H₂O₂ and Ce(SO₄)₂ [24]. In the latter case, the oxygen content increased to 5.04% (H₂O₂) and 4.61% (Ce(SO₄)₂); the tendency of changes in each species of carbon and oxygen atoms is similar to that using nitric acid as the oxidant. From these results, we could not conclude which kind(s) of oxygen containing compound(s) was(were) mainly changed. This is at least in part due to the complicated oxidation reaction. Nevertheless, the surface structure has been changed, i.e. the loosely absorbed oxygen

atoms were removed and replaced with a layer of oxides from the oxidation that bonded more firmly with the carbon structure like the oxidation of activated carbon [29], which is the most important. This is also evident in the weight losses after the oxidation treatments, 9.33% and 1.98% for OA and ON, respectively. If the surface oxides were not removed, oxidation and weight losses could not have happened. During this oxidation, a dense layer of oxides was produced on the surface of natural graphite. In our previously reported experiments [24], we tried to reoxidize the oxidized natural graphite, and found that the weight loss was much less than that from the first treatment, which clearly indicated that the active imperfect structures such as sp³-hybridized carbon atoms, edge carbon atoms and carbon chains existed in the natural graphite and some of them were removed during the above oxidation treatment though their amounts were small and no method has been found to determine them precisely.

EPR spectra of natural graphite of D, OA and ON are shown in Fig. 3. It indicates that the relative intensity of EPR was increased, from $9.79 \times 10^{11}/\text{g}$ (D) to $1.67 \times 10^{12}/\text{g}$ (OA) and $1.02 \times 10^{12}/\text{g}$ (ON). Though their g-factors for radicals are the same, 2.0078, 2.0076 and 2.0079, the shapes of the spectra are different. After the oxidation, it became sharper. In natural graphite, there are several radicals before the oxidation, and their sum appears just like the signal of a single species, but the shape is broad. During the oxidation, of course, the former radicals reacted with oxygen and HNO₃, and produced new radicals. In addition, the mild oxidation eliminated some active structural imperfections such as carbon chains and sp³-hybridized carbon atoms and produced further radicals. Of course, most of these radicals were also

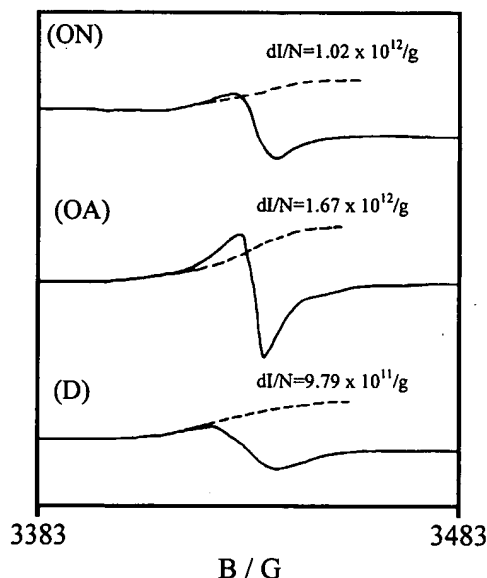


Fig. 3. EPR spectra of natural graphite before (D) and after oxidation by air (OA) and nitric acid solution (ON) measured at room temperature.

situated inside natural graphite [24]. Since they were produced under the same condition, i.e. by the oxidation of oxygen or HNO_3 , the environment for the radicals is almost the same, and thus, the shapes of their EPR spectra are sharper or narrower. This result is evidently different from that using air as an oxidation agent, which shows a sharp decrease in the intensity of electron spinning resonance or the number of radicals [21]. In the latter case [21], the graphite (NG7) is perhaps high in quality, and there are not many imperfections. As a result, a different behavior was observed.

Since some active structural imperfections were eliminated, the structure of the prepared natural graphite became more stable. Curves of thermogravimetry and differential thermal analysis (TG–DTA) of D and ON are shown in Fig. 4. At first, the weight decreased slowly because of the thermal decomposition of some oxides and slight oxidation. When the temperature arrived at above 500 °C, combustion began and the curves of DTA increased. When the combustion proceeded most rapidly, DTA curves peaked. After the oxidation treatment, the exothermal peaks shifted from 742 to 752 °C. This surely suggests that some active sites were removed after the oxidation treat-

ment though the exothermal peak shifted just slightly to a higher temperature, and the graphitic structure became only slightly more stable. It is similar to our results from oxidation with solutions of H_2O_2 and $\text{Ce}(\text{SO}_4)_2$ [24].

HREM micrographs of natural graphite D, OA and ON are shown in Fig. 5. They show an increase in the number of micropores and nanochannels after the oxidation. In the case of air oxidation, nanochannels are clearly identified, and this is similar to what others observed [18]. In the case of oxidation by nitric acid, micropores can be clearly observed. This indicates slightly different oxidation mechanisms, and further study is necessary to identify the specific mechanism. In the case of another strong oxidant $(\text{NH}_4)_2\text{S}_2\text{O}_8$, we also observed a definite increase of micropores from HREM micrographs [30]. However, BET data indicate a slight decrease of the specific surface area, which is consistent with a latter report by Menachem et al. [21]. Later we realized that results of the BET measurement reflected the total specific surface area whereas HREM mainly imaged micropores, corresponding to the inner specific surface area. When the outer specific surface area calculated from the

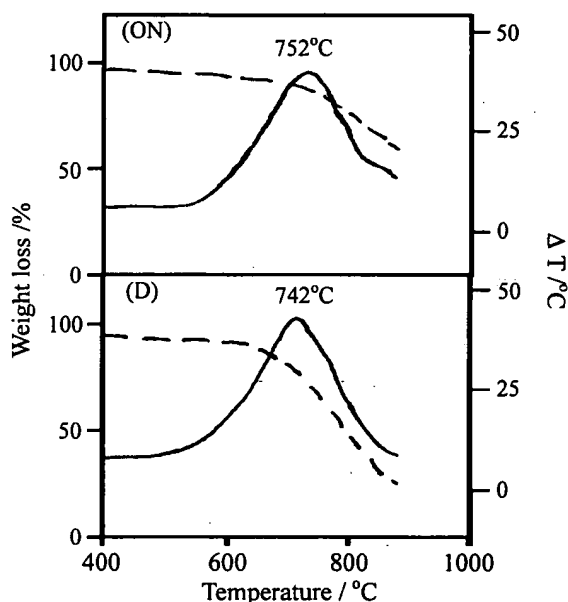


Fig. 4. Diagrams of TG–DTA of natural graphite before (D) and after (ON) the oxidation treatment (---: TG curves; —: DTA curves).

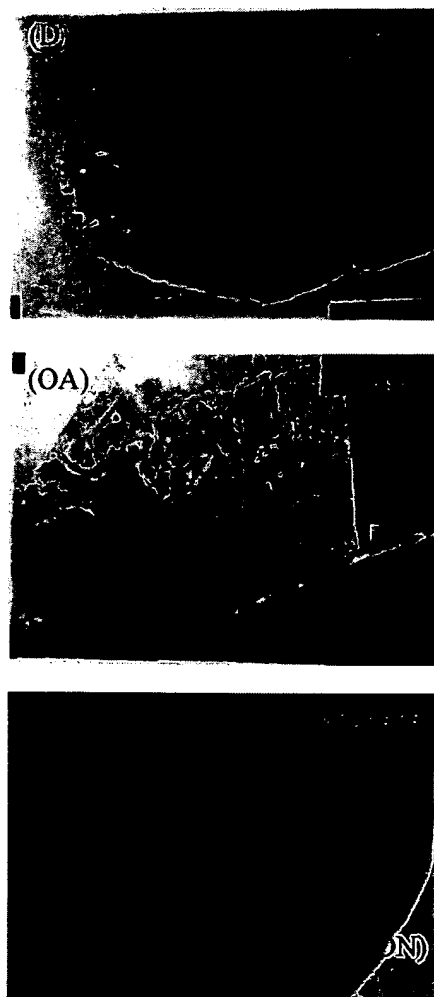


Fig. 5. HREM micrographs of natural graphite before (D) and after oxidation by air (OA) and nitric acid solution (ON) with a length of 310 nm.

distribution of particle diameter was subtracted from the total specific surface area, we got a consistent result, i.e. the inner specific surface area increased after the oxidation treatment. This kind of apparently contradicting phenomenon has never been explained before. Since we also observed an increase in nanochannels and micropores in the cases of O_2 and HNO_3 and the modification actions of HNO_3 and $(NH_4)_2S_2O_8$ are the same, it is assumed that the inner specific surface area will also increase after the oxidation treatment by O_2 and HNO_3 solution.

Discharge and charge profiles in the first cycle and discharge profiles in the second cycle obtained with natural graphite D and the prepared samples OA and ON are presented in Fig. 6. As mentioned above, the electrochemical properties of natural graphite without this treatment were poor. Its reversible capacity was only 251 mAh/g. After the mild oxidation, the reversible capacity increased to 321 mAh/g (OA) and 335 mAh/g (ON), the irreversible capacity above 0.3 V in the first cycle decreased from 56.9 to 55.2 mAh/g (OA) and 21.0 mAh/g (ON). The coulombic efficiency in the first cycle increased from 64% to 78% and 88%, respectively. As indicated above, some reactive structural imperfections were eliminated, consequently, decomposition of electrolyte molecules was diminished [24]. In addition, the surface of natural graphite was covered with a fresh and dense layer of oxides such as hydroxyl/phenol, ether, ester and carbonyl groups. This layer acted as a passivating film when lithium intercalated and blocked the co-intercalation of solvated Li^+ [18,19,24]. Consequently, the coulombic efficiency increased after the oxidation.

The increase of the reversible capacity is mainly due to an increase in the number of nanochannels and micropores caused by the oxidation treatment. Nanochannels and micropores can act as matrices for lithium storage in the forms of lithium molecules or lithium clusters [1,31,32]. They provide inlets and

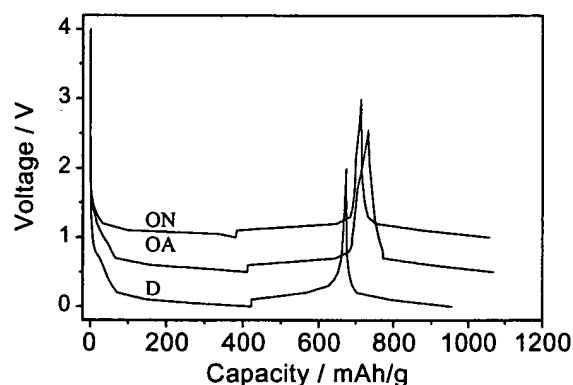


Fig. 6. Discharge and charge profiles in the first cycle and discharge profiles in the second cycle of natural graphite before (D) and after oxidation by air (OA) and nitric acid solution (ON) (for clarity, voltages of OA and ON were shifted upwards by 0.5 and 1.0 V, respectively).

outlets for lithium during discharge and charge and thus favor lithium intercalation and deintercalation.

For a comparison, the graphite TIMREX® SFG44, having a good electrochemical performance before an oxidation treatment, shows only a very small increase of its reversible capacity from 340 to about 350 mAh/g; the coulombic efficiency in the first cycle also increased only slightly from 83.1% to 88.7% [22]. In another report, the reversible capacity of both pristine and modified graphite is below 300 mA h/g although there is an increase of <20% [19]. Peled et al. [18] used Lonza graphite and reported an increase in capacity after oxidation by about 10–30% with a final value around 372 mAh/g. This shows evidently the difference between graphite samples from different sources.

As to the effects of radicals, it is still not clear from our results. At first it was suggested that radicals were possibly involved in reactions with Li and led to an enhancement of reversible capacity [18]. Later it was found that there was a sharp decrease of radicals after oxidation, thus, any correlation between radical concentration and excess capacity is unlikely [21]. In our case, radicals were situated at the inner surface of graphite; they did not cause evident side reactions. As to their specific actions on electrochemical performance, further investigation is necessary.

Cycling behaviors of natural graphite D and the prepared samples OA and ON are presented in Fig. 7. In the case of natural graphite D, the reversible

capacity faded to 105 mA h/g in the first 10 cycles. After the oxidation treatment, its cycling behaviors improved much, and there was no evident fading in the reversible capacity both with graphite treated with O₂ and HNO₃ solution. In the case of synthetic graphite TIMREX® SFG44, its cycling behavior is good and there is no evident fading at least in the reported four cycles. After oxidation, its cycling behavior does not change and there is also no fading [22]. Our results show that the stability of natural graphite structure improved due to the removal of structural imperfections and formation of a dense layer of oxides during the oxidation treatment. Therefore, side reactions such as co-intercalation of solvated lithium ions were blocked, and the movement of graphene planes along the *a*-axis direction became difficult, which also inhibits exfoliation or the disruption of graphite [24]. As a result, good cycling behavior was achieved.

4. Conclusion

In summary, the oxidation treatments of natural graphite containing imperfections by air and nitric acid solution can effectively improve its electrochemical performance as anode materials for lithium ion batteries similar to the treatment with solutions of H₂O₂ and Ce(SO₄)₂ [24]. Through oxidation, some structural imperfections with high reactivity towards lithium such as carbon chains, edge carbon atoms and sp³-hybridized carbon atoms were eliminated, and nanochannels and micropores were introduced. In addition, the surface of natural graphite was modified and recoated with a dense layer of oxides; the stability of graphite structure was increased preventing the decomposition of electrolyte and movement of graphene planes along its *a*-axis direction. Consequently, the reversible capacity enhanced from 251 to 321 and 335 mAh/g, respectively, the coulombic efficiency in the first cycle increased from 64% to 78% and 88%, and the reversible capacity apparently did not fade.

In the case of air oxidation, it is difficult to control the homogeneity and reproducibility of the product since this oxidation reaction happens at a gas–solid interphase. As to the oxidation using nitric acid, the homogeneity can be easily controlled since

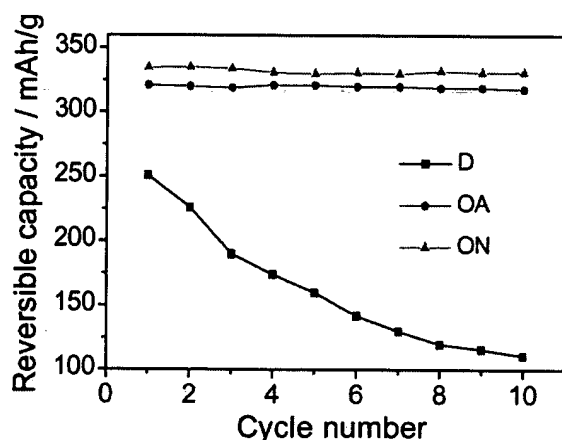


Fig. 7. Cycling behavior of natural graphite before (D) and after oxidation by air (OA) and nitric acid solution (ON).

this is a liquid–solid interface reaction. It can be used to manufacture anode materials for lithium ion batteries on a large scale. There is a production of nitride oxides, which can be recycled by absorption in nitric acid. Our results also suggest that the requirements for the primary material, natural graphite, are not high. The utilization of this kind of common natural graphite will greatly lower the cost of the anode material.

Acknowledgements

Financial support from China Postdoctor Foundation and Alexander von Humboldt Foundation (Y.P.W.) are gratefully acknowledged.

References

- [1] Y.P. Wu, C. Wan, C. Jiang, S.B. Fang, *Principles, Introduction and Advances of Lithium Secondary Batteries*, Tsinghua Univ. Press, Beijing, 2002.
- [2] M. Koh, T. Nakajima, *Electrochim. Acta* 44 (1999) 1713.
- [3] M. Yoshio, H.Y. Wang, K. Fukuda, Y. Hara, Y. Adachi, *J. Electrochem. Soc.* 147 (2000) 1245.
- [4] Y. Sato, Y. Kikuchi, T. Nakano, G. Okuno, K. Kobayakawa, T. Kawai, A. Yokoyama, *J. Power Sources* 81–82 (1999) 182.
- [5] R. Mishima, T. Tsuno, S. Yoon, JP Patent, JP 11-329435 (1999).
- [6] F. Joho, B. Rykart, R. Imhof, P. Nova, M.E. Spahr, A. Monnier, *J. Power Sources* 81–82 (1999) 243.
- [7] S. Yoon, H. Kim, S.M. Oh, *J. Power Sources* 94 (2001) 68.
- [8] Y. Kida, K. Yanagida, A. Funahashi, T. Nohma, I. Yonezu, *J. Power Sources* 94 (2001) 74.
- [9] H. Wang, M. Yoshio, *J. Power Sources* 93 (2001) 123.
- [10] T. Takamura, K. Sumiya, J. Suzuki, C. Yamada, K. Sekine, *J. Power Sources* 81–82 (1999) 368.
- [11] Y.P. Wu, C.Y. Jiang, C.R. Wan, E. Tsuchida, *Electrochem. Commun.* 2 (2000) 626.
- [12] Y.P. Wu, C.Y. Jiang, C.R. Wan, R. Holze, *Carbon*, in press.
- [13] P. Yu, J.A. Ritter, R.E. White, B.N. Popov, *J. Electrochem. Soc.* 147 (2000) 1280.
- [14] H. Huang, E.M. Kelder, J. Schoonman, *J. Power Sources* 97–98 (2001) 114.
- [15] S. Kim, Y. Kadoma, H. Ikuta, Y. Uchimoto, M. Wakihara, *Electrochem. Solid-State Lett.* 4 (2001) A109.
- [16] M. Gaberek, M. Bele, J. Drogenik, R. Dominko, S. Pejovnik, *J. Power Sources* 97–98 (2001) 67.
- [17] M. Saito, K. Sumiya, K. Sekine, T. Takamura, *Electrochemistry* 67 (1999) 957.
- [18] E. Peled, C. Menachem, A. Melman, *J. Electrochem. Soc.* 143 (1996) L4.
- [19] T. Nakajima, K. Yanagida, *Tanso* 174 (1996) 195.
- [20] Y.P. Wu, C.Y. Jiang, C.R. Wan, E. Tsuchida, *Electrochem. Commun.* 2 (2000) 272.
- [21] C. Menachem, Y. Wang, J. Floners, E. Peled, S.G. Greenbaum, *J. Power Sources* 76 (1998) 180.
- [22] T. Takamura, H. Awano, T. Ura, K. Sumiya, *J. Power Sources* 68 (1997) 114.
- [23] H. Buqa, P. Golob, M. Winter, J.O. Besenhard, *J. Power Sources* 97–98 (2001) 122.
- [24] Y.P. Wu, C. Jiang, C. Wan, E. Tsuchida, *J. Mater. Chem.* 11 (2001) 1233.
- [25] L.C.F. Blackman, *Modern Aspects of Graphite Technology*, Academic Press, London, 1970.
- [26] G.C. Chung, S.H. Jun, K.Y. Lee, M.H. Kim, *J. Electrochem. Soc.* 146 (1999) 1664.
- [27] J.P. Olivier, M. Winter, *J. Power Sources* 97–98 (2001) 151.
- [28] U. Zielke, K.J. Huttering, W.P. Hoffman, *Carbon* 34 (1996) 983.
- [29] C. Moreno-Castilla, M.A. Ferro-Garcia, J.P. Joly, I. Bautista-Toledo, F. Carrasco-Marin, J. Rivera-Utrilla, *Langmuir* 11 (1995) 4386.
- [30] Y.P. Wu, C. Jiang, C. Wan, R. Holze, *J. Appl. Electrochem.*, in press.
- [31] Y.P. Wu, C. Wan, C. Jiang, S.B. Fang, Y.Y. Jiang, *Carbon* 37 (1999) 1901.
- [32] A. Mabuchi, T. Katsuhisa, H. Fujimoto, T. Kasuh, *J. Electrochem. Soc.* 142 (1995) 1041.



0008-6223(95)00082-8

EVOLUTION OF MICROTEXTURE IN FURAN RESIN- DERIVED CARBON WITH HEAT-TREATMENT

SEI-MIN PARK, EIICHI YASUDA, TAKASHI AKATSU, YASUHIRO TANABE,

MASATO KAKIHANA

Research Laboratory of Engineering Materials, Tokyo Institute of Technology, 4259, Nagatsuta, Midori,
 Yokohama 226, Japan

and

KAZUHIRO OZAWA

Central Technical Research Laboratory, Nippon Oil Company Ltd, 8, Chidori, Naka, Yokohama 231,
 Japan

(Received 2 September 1994; accepted in revised form 17 March 1995)

Abstract—Microtextural evolution in furan resin-derived carbon was investigated. The evolution was mainly studied from the viewpoint of the change in microtexture of surface and internal pores with heat-treatment and was characterized by observation with a scanning electron microscope, measurement of the BET surface area, X-ray diffraction and Raman spectroscopy. Microporous layers, about 60 μm thick, were formed on the surface during carbonization at 1000°C when furan resin was polymerized in ambient air. The layer partially changed into graphite with a small surface area after heat-treatment at 2600°C, the inside remaining amorphous. The microporous layer was easily rearranged to form a graphite layer, compared to the inside. The carbons that existed in the internal closed pore during heat-treatment at 1000°C changed into turbostratic carbon by heat-treatment at 2600°C. The texture resulted from mass transport through gas phase during the heat-treatment.

Key Words—Furan resin, microtexture, micropore, graphitic layer, internal pore.

1. INTRODUCTION

Thermosetting resins are known to form hard carbons via a solid state carbonization. They are commonly used as matrices of carbon fiber reinforced carbon composite, owing to convenient processing features such as impregnation, shape-holding during carbonization, etc. However, the hard carbons are difficult to graphitize even by heat-treatment at 3000°C. Generally, the high randomness or the highly crosslinked texture similar to glass in hard carbons results from the molecular arrangement or orientation in thermosetting polymers during heat-treatment [1]. Structural models [2,3] have been proposed for these amorphous carbons, which are liquid and gas impermeable. Yamada [4] reported the specific surface area of furan resin-derived carbon powder of 80–100 μm in diameter against heat-treatment temperature (HTT) up to 1300°C. He found that the specific surface area increased up to 800°C with increasing HTT and then decreased, but gas impermeability of bulk material was maintained.

Recently, a few studies reported on graphitization behavior in non-graphitizable carbons. Using a high resolution scanning electron microscope, Hishiyama *et al.* observed that in non-graphitizable carbon films derived from a cellulose film [5] and polyimide film [6], skins 100–300 nm thick were graphitized, but the inside texture remained amorphous. Hatori *et al.* [7,8] also reported that graphitic thin skins were observed on non-graphitizable carbon film derived from polyimide film. They concluded that the graphi-

tizability of a given polymer could be controlled by molecular orientation.

Graphitization of carbon material has generally been characterized through the measurement of mean interlayer spacing d_{002} and mean crystallite size L_c by X-ray diffraction (XRD) and scanning electron microscopy (SEM). Raman scattering [9,10] has been recognized as a useful method for characterization of graphite and diamond. Micro-Raman spectroscopy has recently been developed to analyze microtextures in selected local areas of carbon fibers [11].

In the present paper, carbonization behavior of furan resin and the microstructural evolution in the resin-derived carbon are discussed from the viewpoint of the change in the as-treated surface, inside body and surface of the internal pore with heat treatment at 2600°C through measurements of specific surface area, XRD and Raman spectra, and SEM observation.

2. EXPERIMENTAL PROCEDURES

Furfuryl alcohol condensate (furan resin, Hitafulan 302) was chosen as a carbon origin. The resin was hardened with polymerizing agent, paratoluene sulfonic acid, for one week in ambient air, and then polymerized at 100°C for 96 hours in a drying oven. The polymerized specimens were cut into dimensions of $10 \times 10 \times (2-3) \text{ mm}^3$. Carbonization was carried out at 1000°C for 2 hours in flowing Ar, followed by heat-treatment at 2600°C for 30 minutes in flowing Ar. The specimens, carbonized at 1000°C

and heat-treated at 2600°C, were characterized by the measurements of specific surface area with different levels of burn-off from 0 to 30% and the Raman spectra.

The specific surface area was measured by BET plots from the adsorption-desorption curve of N_2 gas at liquid nitrogen temperature. Ten pieces of specimens were prepared to obtain accurate specific surface area measurements in each heat-treatment. Adsorption of Kr at the same temperature was alternatively carried out to obtain BET plots in the case of small surface area.

The as-heat-treated surface was observed using SEM (JEOL T-100) for the carbonized specimens with different polymerization conditions of the resin at an acceleration voltage of 25 kV. SEM observation was also carried out on internal pores for both of the specimens heat-treated at 1000°C and 2600°C, by the same condition.

Raman scattering spectra were obtained with a triple Raman spectrometer, Atago-Jobin Yvon T64000. An argon laser beam (wavelength 514.5 nm) was used for excitation. The laser beam was focused to a spot about 1 μm in diameter. As Raman scattering is known to be sensitive to mechanical damage such as polishing or grinding [12,13], the surfaces exposed to the laser beam were either as-heat-treated or fractured.

XRD measurement was made using $\text{CuK}\alpha$ radiation on the powders prepared from the specimen heat-treated at 2600°C. The diffraction profile of (002) was obtained using high purity silicon powder as an internal standard.

3. RESULTS AND DISCUSSION

3.1 Microstructure of specimen surface

Figure 1 shows adsorption-desorption curves of nitrogen for the specimens with burn-off of 0 and 36% in weight after carbonization at 1000°C. The

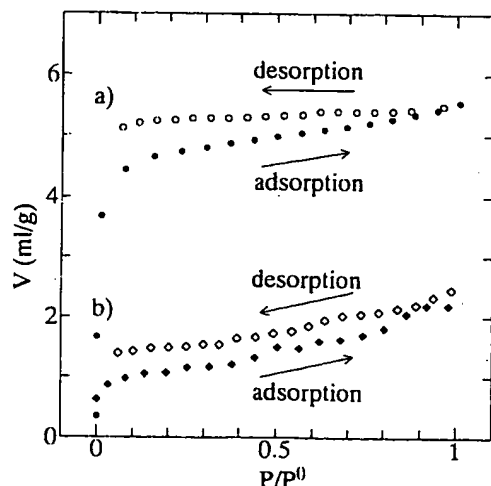


Fig. 1. Adsorption-desorption curves of N_2 (a) for as-carbonized specimen and (b) after a 36% burn-off.

total amount of adsorbate decreased with increase of the amount of burn-off. The curves indicate that the adsorbent includes so many micropores in nanometer scale. The hysteresis observed suggests that the pore size near the surface is narrower than that in the inside, like a bottle neck.

Specific surface area obtained from BET plots is shown in Fig. 2 as a function of burn-off for the carbonized specimens. As the amount of burn-off increased to 2% in the carbonized specimens, specific surface area increased, and then decreased drastically to 10% of burn-off. The value increased again slightly at 36% of burn-off. SEM observation of the surface of the 1000°C-treated specimen showed a burn-off of about 2% (Fig. 3). A surface layer of about 60 μm thick was peeled off from the inside. The layer was microporous but the inside was not. The layer, therefore, had to have a large specific surface area. Taking into consideration the amount of microporous surface layer (60 μm), the amount is 6% in weight, hence the change in specific surface area could be divided into 2 steps. The first is for the extinction of microporous surface layer, the second is for the formation of pits by oxidation below the surface.

The shapes of surface layers that peeled off indicate much shrinkage during carbonization, compared to the inside layers. Savage [14] insisted that if crosslinkage of polymer was too great, large thermal stress could build up during carbonization, which could lead to premature failure. The structural difference between the surface and the inside was considered to originate from a polymerization/polycondensation reaction. The specific surface area of the carbonized specimen after polishing off about 0.2 mm of both sides decreased by up to 2 orders of magnitude as shown in Fig. 2 (open circles), compared to the non-polished specimen (closed circle) at 0% of burn-off. These facts indicate that the formation of the microporous layer was already determined before carbonization.

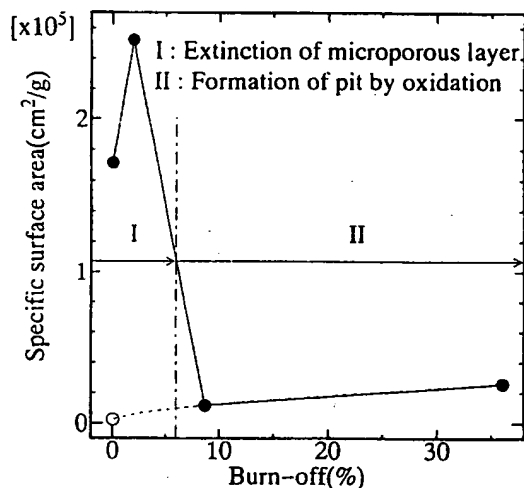


Fig. 2. Change in specific surface area (cm^2/g) as a function of burn-off (%) in carbonized specimens.

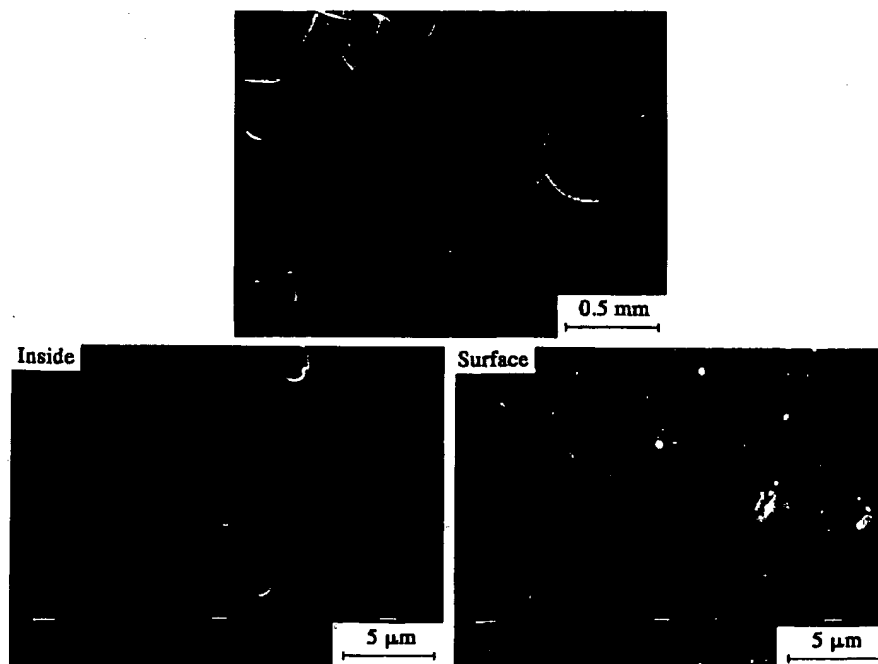


Fig. 3. The surfaces of carbonized specimens after a 2% burn-off.

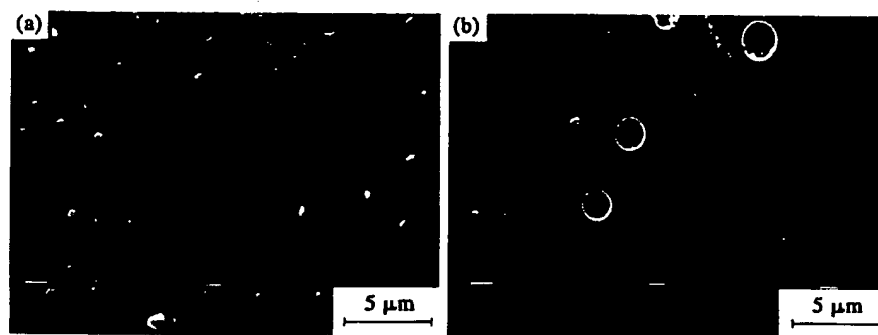


Fig. 4. The difference in surfaces of carbonized specimens polymerized in (a) ambient air and (b) flowing Ar.

In order to confirm the origin of the formation of the microporous layer during carbonization, one more hardening condition was selected. The resin was hardened in flowing Ar gas, and polymerized and carbonized in the same way as hardening in ambient air. SEM micrographs of the specimen are shown in Fig. 4. The micropores in micrometric scale were entirely distributed in the surface region of the specimen carbonized after hardening in air. The micropores could not be observed in the surface region of the specimen carbonized after hardening in flowing Ar. The result suggests that the formation of microporous layer after heat-treatment at 1000°C was determined by chemical reaction in early polymerizing stage with air, with oxygen probably playing an important role in its formation. As an additional experiment, an initially polymerized specimen was prepared in flowing oxygen and then carbonized by the same procedure. The microporous layers peeled off were also observed after burn-off of about 2% of the carbonized specimen. The formation of micro-

porous layers was considerably dependent upon the initial polymerizing atmosphere, especially oxygen.

Specific surface area was considerably decreased to 3 orders of magnitude, by heat-treatment at 2600°C. The values were less than 200 cm²/g, regardless of the amount of burn-off. Adsorption isotherm was hard to obtain even by Kr adsorption for the specimen heat-treated at 2600°C. A little weight change (<0.1%) before and after heat-treatment at 2600°C was measured. The weight loss gives evidence for disappearance of the open pores in the microporous layer by heat-treatment at 2600°C.

3.2 Microstructure of internal pore

Figure 5 shows the difference between the specimens heat-treated at 1000 and 2600°C in microstructure of the internal macropore. The carbon in the internal macropore after carbonization at 1000°C was covered on the surface of the pore as skin during heat-treatment at 2600°C, and fibrous materials were formed in the pore at the same time. The results in

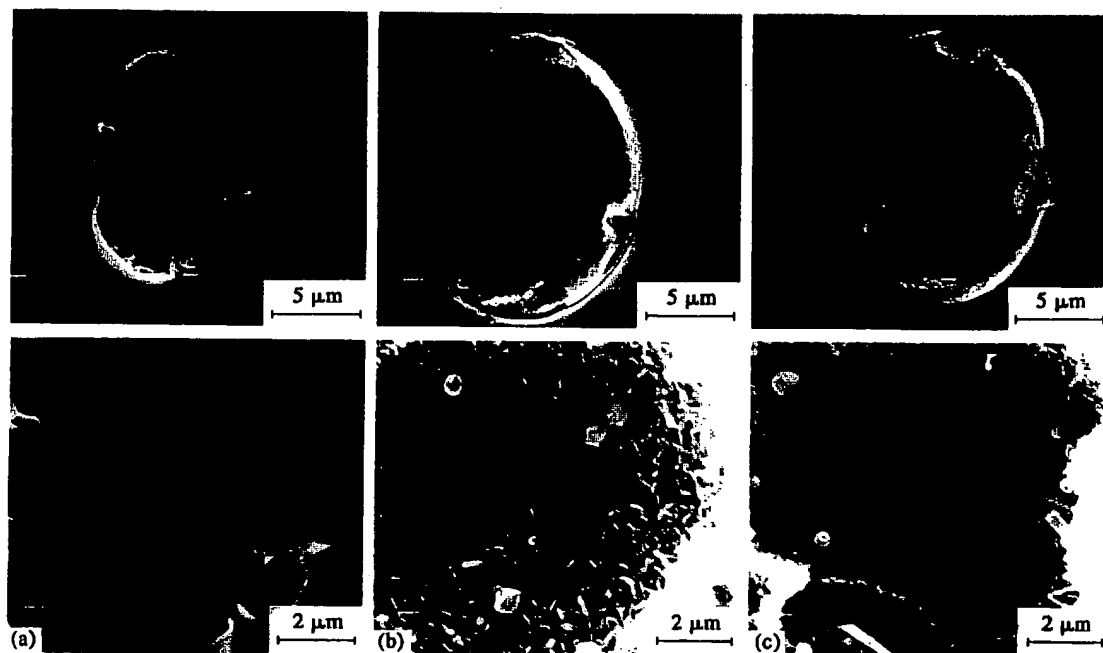


Fig. 5. Microstructure on the surface of internal macropore: (a) HTT 1000°C, (b) and (c) HTT 2600°C.

Fig. 5 imply the possibility of mass transport via the gas phase during heat-treatment.

3.3 Raman spectra and XRD

For the specimens heat-treated at 1000 and 2600°C, Raman scattering spectra were obtained on the fractured surface, internal macropore and as-treated specimen surface, as shown in Figs 6 and 7. Raman scattering at 1580 cm^{-1} corresponds to the characteristic in-plane vibrations of graphite, and that at 1350 cm^{-1} is associated with in-plane vibration caused by structural imperfection. The intensity ratio I_{1350} to I_{1580} is closely related to the mean crystallite size L_a along the a -axis, where I_{1350} and I_{1580} are the intensities at 1350 and 1580 cm^{-1} ,

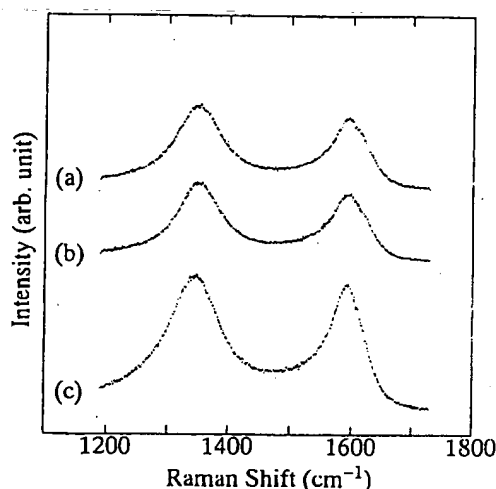


Fig. 6. Raman spectra of the specimens heat-treated at 1000°C: (a) fractured surface, (b) internal macropore surface and (c) as-treated specimen surface.

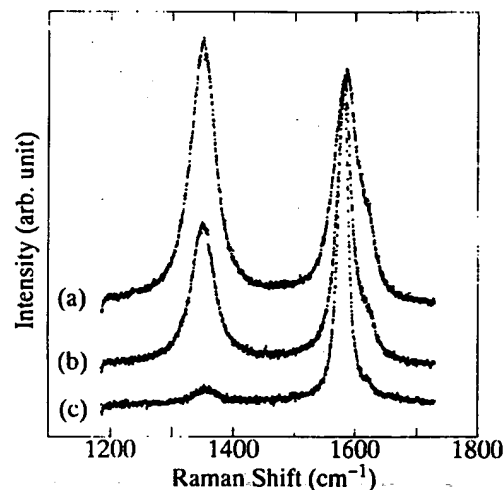


Fig. 7. Raman spectra of the specimens heat-treated at 2600°C: (a) fractured surface, (b) internal macropore surface and (c) as-treated specimen surface.

respectively [15,16]. For the specimen heat-treated at 1000°C, the intensity ratio was a little bit larger than unity, regardless of the region, fractured surface, internal pore and as-treated specimen surface. Therefore, the structure of all regions in the specimen heat-treated at 1000°C can be related to the amorphous structure. The Raman spectra for the specimen heat-treated at 2600°C are very different from those of 1000°C-treated specimens. The intensity ratio obtained was almost zero for the as-treated surface, larger than zero but lower than unity for the internal pore, and a little bit larger than unity for the fractured surface.

The specimen heat-treated at 2600°C exhibits an asymmetrical 002 diffraction profile, which can be

Table 1. XRD parameters d_{002} and L_c , and content of the constituent component for the specimen heat-treated at 2600°C

Component	d_{002} (nm)	L_c (nm)	Content (%)
G	0.336	> 100	1
T	0.342	6	29
B	0.357	3	70

separated into symmetrical profiles under the assumption of coexistence of three different components: graphitic (G), turbostratic (T) and amorphous (B) [17]. XRD parameters d_{002} and L_c , and contents of each component for the specimen heat-treated at 2600°C are listed in Table 1. The microstructures consisted of amorphous carbon for the most parts, with some turbostratic carbon and a negligible amount of graphite. Considering XRD data for the specimen heat-treated at 2600°C and the penetration depth of the laser beam in carbon materials estimated to be 100 nm [18], the as-treated surface consisted of graphite layers with large L_c in submicrometric thickness and the internal pore surface was covered by a skin with a turbostratic structure. The intensity ratio for the fractured surface indicates its amorphous structure.

4. CONCLUSIONS

A microporous layer about 60 μm thick was formed for the specimen of furan resin-derived carbon, heat-treated at 1000°C, when furan resin was polymerized in air. The phenomenon is associated with the chemical reaction between the resin and ambient air, especially oxygen. The microporous layer was rearranged into graphitic layers by heat-treatment at 2600°C, but the inside remained amorphous. The carbon that existed in the internal closed macropore after carbonization at 1000°C was rearranged into

the skin with turbostratic structure and was covered on the surface of the pore by heat-treatment at 2600°C. Rearrangement proceeded by mass transport through the gas phase in the pore.

REFERENCES

1. Y. Yamashita, In *Introduction to Carbon Materials* (in Japanese), pp. 13–27. Carbon Society of Japan, Tokyo (1984).
2. M. Shiraishi, In *Introduction to Carbon Materials* (in Japanese), pp. 29–40. Carbon Society of Japan, Tokyo (1984).
3. G. M. Jenkins and K. Kawamura, *Polymeric Carbons*. Cambridge University Press, London (1976).
4. S. Yamada, *Science for New Engineering Materials, Carbon and Graphite Products* (in Japanese), pp. 265–303. Kinbara Pub. Ltd (1964).
5. Y. Hishiyama, A. Yoshida and Y. Kaburagi, *Carbon* **31**, 1265 (1993).
6. Y. Hishiyama, Y. Kaburagi, A. Yoshida and M. Inagaki, *Carbon* **31**, 773 (1993).
7. H. Hatori, Y. Yamada and M. Shiraishi, *Carbon* **30**, 763 (1992).
8. H. Hatori, Y. Yamada and M. Shiraishi, *Carbon* **31**, 1307 (1993).
9. C. Galiotis and D. N. Batchelder, *J. Mater. Sci. Lett.* **7**, 545 (1988).
10. L. Nikiel and P. W. Jagodzinski, *Carbon* **31**, 1313 (1993).
11. A. W. P. Fung, A. M. Rao, K. Kuriyama, M. S. Dresselhaus, M. Endo and N. Shindo, *J. Mater. Res.* **8**, 489 (1993).
12. R. J. Nemanich and S. A. Solin, *Phys. Rev.* **B20**, 15 (1979).
13. M. Nakamizo, H. Honda and M. Inagaki, *Carbon* **16**, 281 (1978).
14. G. Savage, *Carbon-Carbon Composites*, pp. 117–56. Chapman & Hall, New York (1992).
15. B. T. Kelly, *Physics of Graphite*, pp. 320–22. Applied Science Publishers, London (1981).
16. F. Tuinstra and J. L. Koenig, *J. Comp. Mat.* **4**, 492 (1970).
17. M. Inagaki and K. Kamiya, *Tanso* **71**, 135 (1972).
18. J. Matsui, *Development and Evaluation of Carbon Fiber*, Advanced Carbon Series 1, pp. 122–5. Carbon Society of Japan, Tokyo (1988).



ELSEVIER

Solid State Ionics 80 (1995) 291–298

**SOLID
STATE
IONICS**

Electrochemical intercalation of lithium into graphitized carbons

Asako Satoh, Norio Takami, Takahisa Ohsaki

Materials and Devices Labs., R&D Center, Toshiba Corporation, 1, Komukai Toshiba-cho, Saiwai-ku, Kawasaki 210, Japan

Received 27 April 1995; accepted for publication 17 May 1995

Abstract

The change of the carbon structure with electrochemical intercalation of lithium has been investigated by X-ray diffraction (XRD) method. Graphitized carbons showed the first and the second stage structures clearly during the intercalation process. However, the layer spacing corresponding to the 1st stage structure of graphitized carbon was smaller than that of graphite. This is because the first stage structure of graphitized carbon is the mixed structure of lithiated graphite crystallites and lithiated turbostratic disordered layers. The lithium is mainly intercalated into turbostratic disordered layers above 0.1 V versus Li/Li^+ , and intercalated into graphite crystallites rather than turbostratic disordered layers below 0.1 V versus Li/Li^+ .

Keywords: Lithium battery; Carbon anode; Lithium intercalation; Graphitized carbon

1. Introduction

Electrochemical lithium intercalation into graphites as anodes for lithium batteries has been studied since the early 1980s, and various carbon materials have been proposed as good candidates for anodes in secondary lithium batteries [1–7]. These carbons show a variety of properties, structures and electrochemical characteristics.

Carbon materials can be distinguished into two types, graphitized carbon and disordered carbon, on the basis of the crystal structure [8]. Graphitized carbons are characterized as graphite structures including some turbostratic disordered layers which are stacked with random translations and rotations between adjacent carbon hexagonal layers. Disordered carbons are made up of small crystallites which have buckled turbostratic disordered structures [9] and unorganized carbons connecting each crystallite.

Electrochemical behavior, capacity, voltage, kinetics and stability in organic solvents for carbons during lithium intercalation and deintercalation already have been studied by several researchers [1–7,10–16]. In particular, Dahn and co-workers [13] have reported the relationship between host carbon structure and the maximum lithium intercalation capacity in detail. However the structural change and the lithium intercalation mechanism in carbons have not been well explained except for graphite. Also the electrochemical intercalation into various graphitized carbons with different graphitization degrees has not been well characterized yet. In this paper, the lithium intercalation into graphitized carbons was investigated in order to reveal characteristics of graphitized carbons as anodes. The structural changes for graphitized carbons during the lithium intercalation were studied by the ex-situ X-ray diffraction method. The dependence of the lithium intercalation on the host carbon layer structure is discussed.

2. Experimental

2.1. Carbons

Seven carbon samples were used for this study. Of these, one was artificial graphite (KS44) prepared by Lonza Co., Ltd., one was heat treated resin (HTR) prepared by Mitsubishi Petrochemical Co., Ltd, two were mesophase-pitch-based spherical carbons (meso-carbon microbeads, MCMB) prepared by Osaka Gas Co., Ltd, and the rests were mesophase-pitch-based carbon fibers (MPCF) prepared by Petoca Co., Ltd, which were heat-treated in the temperature range of 2000–3000°C. Heat-treatment temperature (HTT) and structural parameters are summarized in Table 1. The authors divided these graphitized carbons into three types by d_{002} value, average spacing of carbon layers, as shown in Table 1. Graphite consists of large crystallites where the adjacent carbon hexagonal layers have the typical ABABAB... stacking arrangement. Turbostratic disordered carbon consists of rather small crystallites and all carbon layers are stacked turbostratically. Graphitized carbon is a mixture of both graphite-type crystallites and turbostratic disordered layers. The ratio of the two kinds of stacking arrangement determines d_{002} .

2.2. Electrochemical cell construction

Electrochemical intercalation was carried out in a three-electrode glass cell with lithium metal as a counter electrode and reference electrode. Working electrodes were made from carbon powder mixed with 3 wt% of Teflon and spread onto $2 \times 2 \text{ cm}^2$ sus-

mesh, and dried at 140°C under vacuum for at least 12 h before use. All experiments were carried out at 24–25°C in a dry argon atmosphere. The authors used the solution of 1 M LiPF_6 in ethylene carbonate (EC)/propylene carbonate (PC) mixed solvent as the electrolyte in this study. All electrolytes were used as received because they were battery grade products (Tomiyaama pure chemical Co., Ltd.). The charge (intercalation)–discharge (deintercalation) characteristics of carbon electrodes were evaluated using galvanostatic cycling at a constant current of $i = 0.25 \text{ mA/cm}^2$ between 0 and 1 V versus Li/Li^+ .

2.3. Ex-situ X-ray diffraction analysis

Powder X-ray diffraction profiles of carbon electrodes and lithium intercalated carbon electrodes were collected by using a Rigaku diffractometer, equipped with a copper target X-ray tube and a diffracted beam monochromator. The cell was disassembled under Ar atmosphere and carbon electrode was washed with acetonitrile to remove the electrolyte on the electrode surface and dried. The authors measured the change of carbon structure during the second cycle with the intercalation process to avoid the influence of the electrolyte decomposition during the first cycle [5]. The electrode sample was sealed with the thin film to avoid the sample decomposition with air and water. Reflection-free quartz sample plate was used.

3. Results and discussion

3.1. Voltage profiles and capacities

Fig. 1 shows the electrochemical intercalation voltages of graphite (KS44) and MPCF heated at 3000°C and 2000°C at the second cycle. The gradient of voltage curve for graphite changes remarkably at three points. These points are marked in the figure at the charge capacities of 20, 70, and 190 mAh/g, respectively. These charge capacities are corresponding to $x = 0.05$, 0.19 and 0.51 in Li_xC_6 . The gradient for MPCF heated at 3000°C also changes at 30, 80, 180 mAh/g corresponding to the x values, 0.08, 0.22 and 0.48 in Li_xC_6 respectively. These changes of the curve for MPCF heated at 3000°C are smooth

Table 1
Carbon samples used in this work

Carbon type	No.	HTT (°C)	d_{002} (nm)	L_c (nm)	L_a (nm)
Graphite	KS44		0.3358	> 100	> 100
	HTR		0.3365	> 100	> 100
Graphitized carbon	MCMB1	2800	0.3372	36	97
	MPCF	3000	0.3379	32	84
	MPCF	2300	0.3394	16	12
Turbostratic disordered carbon	MCMB2		0.3429	16	10
	MPCF	2000	0.3435	11	11

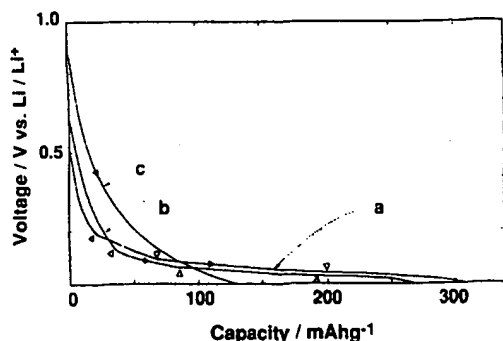


Fig. 1. The voltage profiles for various types of carbon in the lithium intercalation process: (a) KS44, (b) MPCF heated at 3000°C and (c) MPCF heated at 2000°C.

compared with those of graphite. On the other hand, for MPCF heated at 2000°C, the voltage changes smoothly with lithium intercalated capacity, and the maximum capacity is less than that of MPCF heated at 3000°C. The curve of graphite and MPCF heated at 2000°C crosses near 0.1 V versus Li/Li⁺. The lithium intercalation capacity of turbostratic disordered carbon is larger than that of graphite above 0.1 V versus Li/Li⁺, and the capacity of graphite is much larger than that of turbostratic disordered carbon below 0.1 V versus Li/Li⁺.

The variation of the capacity with the average layer spacing of host carbons is shown in Fig. 2. The minimum capacity was obtained near 0.344 nm. This spacing value corresponds to that for turbostratic disordered carbon.

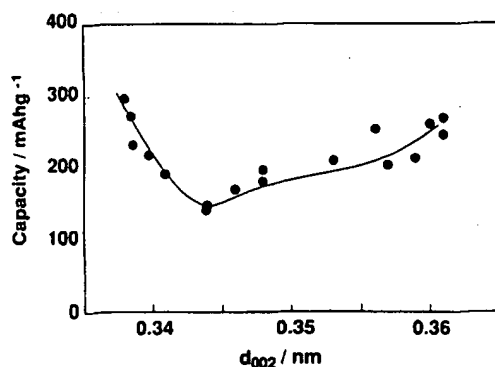


Fig. 2. The variation of discharge capacity for the average layer spacing of the host carbon. In 1 M LiPF₆-EC/PC electrolyte system.

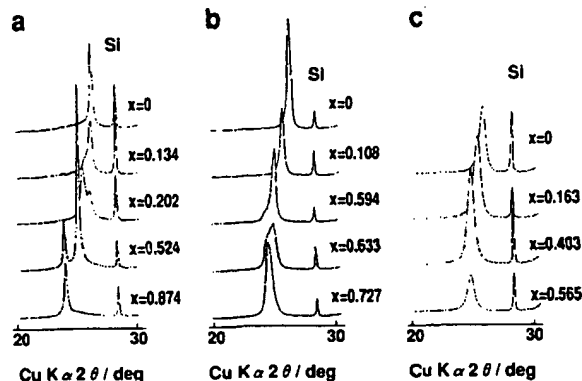


Fig. 3. The changes of the X-ray diffraction profiles for (a) KS44, (b) MPCF heated at 3000°C and (c) MPCF heated at 2000°C.

3.2. X-ray diffraction profiles

Fig. 3 shows the change of the X-ray diffraction profiles for the graphite and MPCF heated at 3000°C and 2000°C with the lithium intercalation in 1M LiPF₆-EC/PC(2:1) electrolyte system. In the profiles for graphite, the first peak position at $x = 0$ in Li_xC₆ corresponded to the (002) Bragg peak of graphite. Then the peak position shifts to a slightly lower angle. The new Bragg peaks grow at $x = 0.202$ and $x = 0.524$, which indicates the formation of some stage structures [17]. The new peak is observed also in the case of MPCF heated at 3000°C at $x = 0.633$. It indicates the existence of a low stage structure though peak charge is more featureless than graphite. On the contrary, the peak shifted smoothly to the lower angle with lithium intercalation in the case of MPCF heated at 2000°C, which indicates a single-phase intercalation [10].

3.3. Graphite

Fig. 4 shows the change of average layer spacing for the graphite with the capacity during the lithium intercalation process in the solvent EC/PC(2:1). The average layer spacing is almost constant at 0.3361–0.3366 nm for $x = 0 - 0.08$ in Li_xC₆, then increases to 0.3523 nm with the discrete points at 0.3484 nm and 0.3446 nm. The value, 0.3523 nm, is maintained and began to exchange to 0.3703 nm from nearly $x = 0.5$. These average spacing values corresponded to the theoretical values for the 1–4th

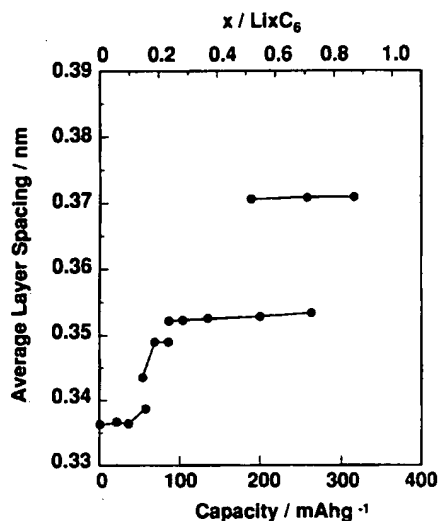


Fig. 4. The changes of the average layer spacing for the KS44 with the lithium intercalation capacity. Solid lines are guides to the eye.

stage structures, which are 0.3706, 0.3527, 0.3467 and 0.344 nm, respectively [18].

This behavior is different from the case of using 12 crown 4 as inhibitor of solvation around lithium [2]. It was reported that the solvation for lithium caused the electrolyte decomposition on the surface of graphite at the first cycle in the PC containing electrolyte systems [5]. The initial plateau, the region of $x = 0-0.05$ in Fig. 4, is considered to indicate the electrolyte decomposition, which shows that the EC/PC electrolyte system is decomposed even at the second cycle. It seems that the following structure variation suffered no serious influence from the electrolyte.

3.4. Turbostratic disordered carbons

The changes of the average layer spacing for turbostratic disordered carbons are indicated in Fig. 5. The linear increase of average layer spacing indicates the absence of stage structures. The peak width also indicated no systematic change. The intercalation stopped near $x = 0.4-0.5$, and the spacing was about 0.36 nm. Dahn et al. [10] have explained that the rotationally disordered host carbon structure affects the maximum capacity of lithium intercalation, and that the structure intercalates lithium to the random site between layers.

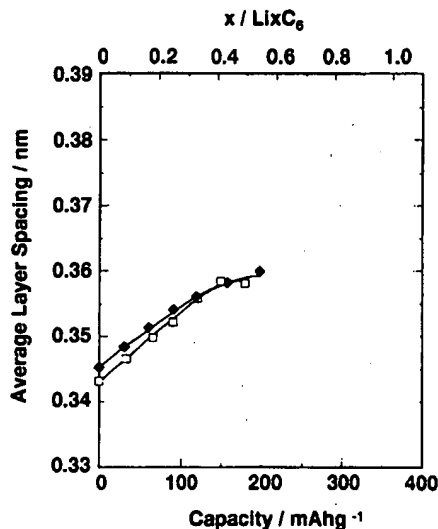


Fig. 5. The changes of the average layer spacing for the carbons mainly consist of turbostratic disordered layers with the lithium intercalation capacity: (♦) MCMB2; (□) MPCF heated at 2000°C.

3.5. Graphitized carbon

Fig. 6 shows the change of the average layer spacing and the peak width of the X-ray diffraction peak for the graphitized carbon, MPCF heated at

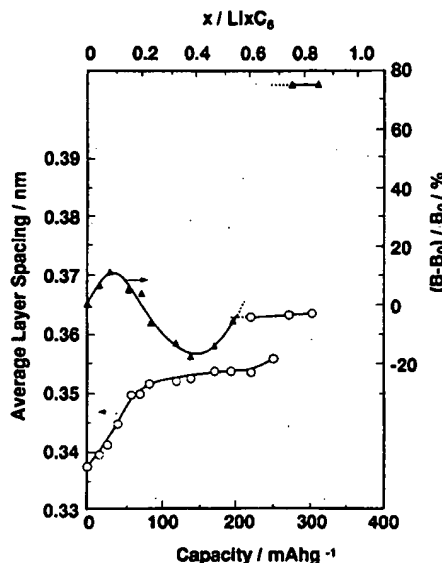


Fig. 6. The changes of the average layer spacing and the peak width of the X-ray diffraction peak for MPCF heated at 3000°C with the lithium intercalation capacity. B is the full width at half maximum of the peak and B_0 is initial value of B .

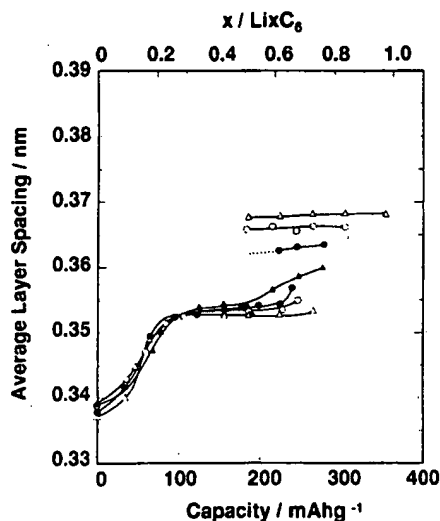


Fig. 7. The changes of the average layer spacing for some graphitized carbons: (Δ) HTR; (\circ) MCMB1; (\bullet) MPCF heated at 3000°C, and (\blacktriangle) MPCF heated at 2300°C.

3000°C, with the capacity during the lithium intercalation. The average layer spacing increases continuously to 0.352 nm (the second stage value) with the increasing of x in Li_xC_6 up to $x = 0.22$, and maintains the value between 0.352 and 0.354 nm in the range of $x = 0.22$ –0.48. The new stage corresponding to the first stage of graphite is observed for $x > 0.5$. The average layer spacing value of this first stage-like structure is 0.3635 nm. The peak width of the X-ray diffraction profile has the maximum point at $x = 0.08$. Discontinuous increasing of the peak width is shown with the formation of the first stage-like structure. No decomposition of electrolytes was observed at second cycle even in the EC/PC elec-

trolyte system, and the difference of solvent systems had no influence on the structural changing.

The graphitized carbon behavior is different from the graphite and turbostratic disordered carbon at three points as follows. Firstly, MPCF heated at 3000°C showed the increase in the layer spacing for $x < 0.22$ without discrete points indicating the stage structures. This suggests that significant amount of lithium is intercalated into turbostratic disordered layers in this region. And the peak width behavior is interpreted as the evidence of high stage structure in the graphite crystallites. Secondly, the average layer spacing increased slightly with the lithium intercalation in the region of $x = 0.2$ –0.5 because of the influence of lithium intercalation into turbostratic disordered layers. In this region, the charge voltage is near 0.1 V versus Li/Li^+ , and lithium can be intercalated into graphite crystallites as much as turbostratic disordered layers. Lastly, the average layer spacing value observed for $x > 0.5$ was significantly smaller than that of graphite. It is because this value is the average of the first stage layer spacing of graphite and lithiated turbostratic disordered layers in proportion to each structure existing in this graphitized carbon.

The voltage curve for MPCF heated at 3000°C changes the gradient at three points as shown in Fig. 1. The capacities of these points correspond to that for maximum point of the peak width ($x = 0.08$), appearance points of the second stage ($x = 0.22$) and the first stage ($x = 0.5$), respectively.

Fig. 7 shows the changes of the average layer spacing for some graphitized carbons. The d_{002} 's of host carbons were intermediate values between those of graphite (0.3354 nm) and turbostratic disordered

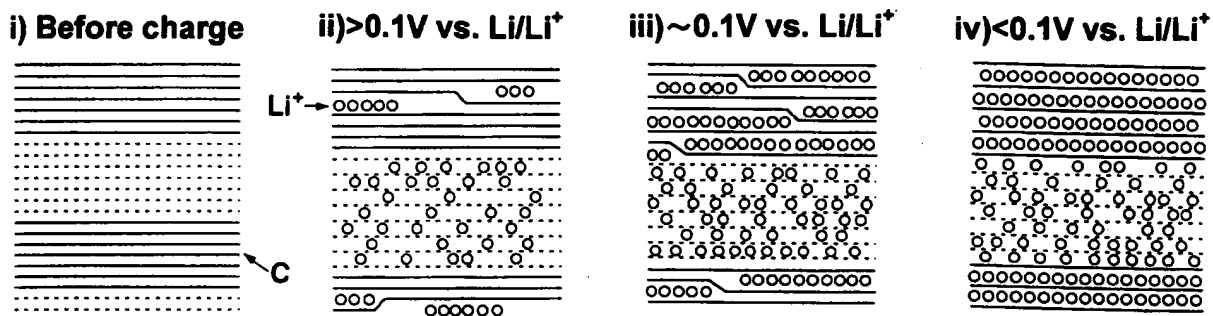


Fig. 8. The schematic drawings of the lithium intercalation into graphitized carbon with charge voltage range. Graphite layers are displayed with solid lines and turbostratic disordered layers with dash lines.

carbon (0.344 nm). These values increased in the order of HTR < MCMB1 < MPCF heated at 3000°C < MPCF heated at 2300°C. They show an intermediate behavior between graphite and turbostratic disordered carbon. The structural changes become smooth and featureless with the d_{002} of host carbon enlarging.

3.6. The model scheme of lithium intercalation

From the experimental results, it is considered that the lithium is competitively intercalated into the graphite-like crystallites and turbostratic disordered stacking layers existing in the host graphitized carbon. The model scheme is displayed in Fig. 8 and explained as follows:

(i) The host graphitized carbon consists of the stacking structure of graphite crystallites (solid line) and turbostratic disordered layers (dash line). The average layer spacing of graphitized carbon is the average of the two kinds of layer spacings of these layer structures in proportion to each carbon layers [8].

(ii) Next, turbostratic disordered layers intercalate lithium principally for $x < 0.2$.

(iii) Then, in the region of $x = 0.2–0.5$, the liquid-like second stage structure in the graphite crystallites intercalates lithium and forms the second

stage of LiC_{12} stoichiometry [1,7]. This voltage is about 0.1 V versus Li/Li^+ . Turbostratic disordered layers intercalate less lithium than graphite crystallites below 0.1 V versus Li/Li^+ .

(iv) In the region below 0.1 V versus Li/Li^+ ($x > 0.5$), lithium is intercalated into graphite crystallites rather than turbostratic layers, because turbostratic structure has less available site for the lithium intercalation than graphite structure in this voltage region.

3.7. Relationship between average layer spacing of host carbon and lithiated carbon

The authors assumed the relationship between the average layer spacing of the host carbon (d_h) and the lithiated carbon illustrated in Fig. 8-iv) (d_{iv}) from the above model, such that

$$d_{iv} = (x' - y')d_h / (x - y) - (x'y - yy') / (x - y) + y', \quad (1)$$

where x is the layer spacing of ideal graphite structure, 0.3354 nm; y is the theoretical layer spacing of ideal turbostratic disordered structure, 0.344 nm [8]; x' is the layer spacing of the first stage structure for the graphite-lithium intercalation compound, 0.3706 nm; and y' is that for turbostratic structure saturated with lithium. The layer spacing obtained from X-ray diffraction peak is the average of layer spacing of carbon layer structures included in the host carbon, and the probability of the existence of each layer structure is calculated from the graphitization degree. The authors used the parameter proposed by Mering et al. [18] to represent the graphitization degree. The values x , x' , y and y' are constant. D_h should be proportional to d_{iv} .

The experimental values of d_{iv} versus d_h are plotted in Fig. 9. The proportional relation between d_{iv} and d_h is shown. This result suggests that the theoretical capacity of graphitized carbon is estimated by the structure of the host carbon and is the sum of the capacity in proportion to each carbon structure, graphite crystallite and turbostratic disordered layer found in the host carbon [13]. The graphite crystallites have the lithium intercalation capacity of 372 mAh/g and LiC_6 structure, while the turbostratic layers have the capacity for the ideal

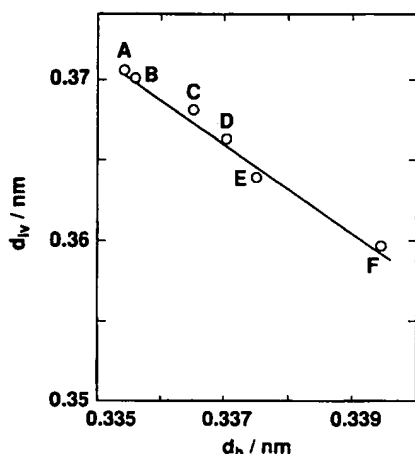


Fig. 9. Relation between average layer spacing of host carbon (d_h) and that of lithiated carbon (d_{iv}): (A) theoretical value; (B) KS44; (C) HTR; (D) MCMB1; (E) MPCF heated at 3000°C, and (F) MPCF heated at 2300°C. Solid line is guide to the eye.

turbostratic disordered structure. The d_{iv} value for the ideal turbostratic disordered carbon calculated from this slope was 0.347 nm which is much smaller than the measurement value, 0.358 nm, for MPCF heated at 2000°C. The reasons for this disagreement are considered to be as follows:

(1) The host carbon, MPCF heated at 2000°C, includes not only the turbostratic disordered carbon but also the unorganized carbon.

(2) The ideal turbostratic structure never exists because of the high lattice strain appeared in the region of $d_{002} > 0.342$ nm [9].

(3) The effect of macrostructure (orientation, the shape of particles and so on).

Recently, Tao Zheng and co-workers [19] reported the effect of turbostratic disorder in graphitic carbon hosts on the intercalation of lithium. They proposed a simple model to explain the relation between lithium ion capacity and graphitization degree of host carbon materials, and they suggested that the interlayer spaces or galleries between randomly stacked layers did not host lithium ions. On the contrary, our experimental results suggested that turbostratic disordered layers intercalated lithium ions and expanded their layer spacing from 0.344 nm to 0.347 nm. This expansion is small and the lithium intercalation capacity of turbostratic disordered layers is considered to be small. Furthermore, the insertion of disordered carbon cannot be neglected for carbon low heat treated at about 2000°C. More careful studies are needed to explain the structural change behavior of turbostratic disordered carbons.

The authors are now investigating the structural change and electrochemical behavior of highly disordered soft carbon with lithium intercalation.

4. Conclusion

The change of carbon layer structure with the electrochemical lithium intercalation for the various host carbon structures were studied by the X-ray diffraction method.

The carbons used in this study are divided into three types: graphite, graphitized carbon and turbostratic disordered carbon. On the basis of the structure change of graphitized carbons during the lithium intercalation, this reaction is explained as the

competitive lithium intercalation into graphite crystallites and turbostratic disordered layers. The lithium is mainly intercalated into turbostratic disordered layers above 0.1 V versus Li/Li⁺. On the contrary, the great amount of lithium intercalated below 0.1 V versus Li/Li⁺ is in graphite crystallites because the intercalation capacity of graphite crystallites in this voltage range becomes much larger than that of turbostratic disordered layers.

The average layer spacing of lithiated graphitized carbon is the average of those for each carbon layer structure existing in the carbon. Therefore, the theoretical lithium intercalation capacity of graphitized carbons is the sum of the calculated capacity in proportion to each carbon layer structure. The maximum capacity is given by the ideal graphite structure.

Acknowledgements

The authors wish to thank Dr. Motoya Kanda for guidance and discussion during the course of this research. Toshiba Corporation assisted in meeting the publication costs of this article.

References

- [1] R. Yazami and Ph. Touzain, *J. Power Sources* 9 (1983) 365.
- [2] J.R. Dahn, *Phys. Rev. B* 44 (1991) 9170.
- [3] Z.X. Shu, R.S. McMillan and J.J. Murray, *J. Electrochem. Soc.* 140 (1993) 922, L101.
- [4] D. Billand, F.X. Henry and P. Willmann, *Mat. Res. Bull.* 28 (1993) 477.
- [5] R. Fong, U. von Sacken and J.R. Dahn, *J. Electrochem. Soc.* 137 (1990) 2009.
- [6] D. Guyomard and J.M. Tarascon, *J. Electrochem. Soc.* 139 (1992) 937.
- [7] T. Ohzuku, Y. Iwakoshi and K. Sawai, *J. Electrochem. Soc.* 140 (1993) 2490.
- [8] R.E. Franklin, *Proc. Roy. Soc. A* 209 (1951) 196.
- [9] M. Inagaki, *J. Appl. Cryst.* 5 (1972) 295.
- [10] J.R. Dahn, R. Fong and M.J. Spoon, *Phys. Rev. B* 42 (1990) 6424.
- [11] A.K. Sleight and U. von Sacken, *Solid State Ionics* 57 (1992) 99.
- [12] N. Imanishi, H. Kashiwagi, T. Ichikawa, Y. Takeda, O. Yamamoto and M. Inagaki, *J. Electrochem. Soc.* 140 (1993) 315.

- [13] J.R. Dahn, A.K. Sleight, Hang Shi, J.N. Reimers, Q. Zhong and B.W. Way, *Electrochim. Acta* 38 (1993) 1179.
- [14] T. Kitamura, T. Miyazaki, T. Kawagoe, T. Kita and T. Matsunaga, *Synth. Met.* 18 (1987) 537.
- [15] R. Kanno, Y. Kawamoto, Y. Takeda, S. Ohashi, N. Imanishi and O. Yamamoto, *J. Electrochem. Soc.* 139 (1992) 3397.
- [16] N. Takami, A. Satoh, M. Hara and T. Ohsaki, *J. Electrochem. Soc.* 142 (1995) 371.
- [17] D. Guerard and A. Herold, *Carbon* 13 (1975) 337.
- [18] Mering and Maire, *Les Carbons* 1 (1965) 129.
- [19] Tao Zheng, J.N. Reimers and J.R. Dahn, *Phys. Rev. B* 51 (1995) 734.

**This Page is Inserted by IFW Indexing and Scanning
Operations and is not part of the Official Record**

BEST AVAILABLE IMAGES

Defective images within this document are accurate representations of the original documents submitted by the applicant.

Defects in the images include but are not limited to the items checked:

- ☐ BLACK BORDERS
- ☐ IMAGE CUT OFF AT TOP, BOTTOM OR SIDES
- ☒ FADED TEXT OR DRAWING
- ☒ BLURRED OR ILLEGIBLE TEXT OR DRAWING
- ☐ SKEWED/SLANTED IMAGES
- ☐ COLOR OR BLACK AND WHITE PHOTOGRAPHS
- ☐ GRAY SCALE DOCUMENTS
- ☒ LINES OR MARKS ON ORIGINAL DOCUMENT
- ☒ REFERENCE(S) OR EXHIBIT(S) SUBMITTED ARE POOR QUALITY
- ☐ OTHER: _____

IMAGES ARE BEST AVAILABLE COPY.

As rescanning these documents will not correct the image problems checked, please do not report these problems to the IFW Image Problem Mailbox.